JOURNAL OF GEOPHYSICAL RESEARCH, VOL. 113, D10206, doi:10.1029/2007JD009769, 2008



# Using observations of deep convective systems to constrain atmospheric column absorption of solar radiation in the optically thick limit

Xiquan Dong,[1] Bruce A. Wielicki,[2] Baike Xi,[1] Yongxiang Hu,[2] Gerald G. Mace,[3] Sally Benson,[3] Fred Rose,[4] Seiji Kato,[2] Thomas Charlock,[2] and Patrick Minnis[2]

Received 28 December 2007; revised 28 December 2007; accepted 31 January 2008; published 29 May 2008.

[1] Atmospheric column absorption of solar radiation ($A_{col}$) is a fundamental part of the Earth's energy cycle but is an extremely difficult quantity to measure directly. To investigate $A_{col}$, we have collocated satellite-surface observations for the optically thick Deep Convective Systems (DCS) at the Department of Energy Atmosphere Radiation Measurement (ARM) Tropical Western Pacific (TWP) and Southern Great Plains (SGP) sites during the period of March 2000–December 2004. The surface data were averaged over a 2-h interval centered at the time of the satellite overpass, and the satellite data were averaged within a $1^\circ \times 1^\circ$ area centered on the ARM sites. In the DCS, cloud particle size is important for top-of-atmosphere (TOA) albedo and $A_{col}$ although the surface absorption is independent of cloud particle size. In this study, we find that the $A_{col}$ in the tropics is ~0.011 more than that in the middle latitudes. This difference, however, disappears, i.e., the $A_{col}$ values at both regions converge to the same value (~0.27 of the total incoming solar radiation) in the optically thick limit ($\tau > 80$). Comparing the observations with the NASA Langley modified Fu_Liou 2-stream radiative transfer model for optically thick cases, the difference between observed and model-calculated surface absorption, on average, is less than 0.01, but the model-calculated TOA albedo and $A_{col}$ differ by 0.01 to 0.04, depending primarily on the cloud particle size observation used. The model versus observation discrepancies found are smaller than many previous studies and are just within the estimated error bounds. We did not find evidence for a large cloud absorption anomaly for the optically thick limit of extensive ice cloud layers. A more modest cloud absorption difference of 0.01 to 0.04 cannot yet be ruled out. The remaining uncertainty could be reduced with additional cases, and by reducing the current uncertainty in cloud particle size.

**Citation:** Dong, X., B. A. Wielicki, B. Xi, Y. Hu, G. G. Mace, S. Benson, F. Rose, S. Kato, T. Charlock, and P. Minnis (2008), Using observations of deep convective systems to constrain atmospheric column absorption of solar radiation in the optically thick limit, *J. Geophys. Res.*, *113*, D10206, doi:10.1029/2007JD009769.

## 1. Introduction

[2] In the last few decades, our knowledge of the radiation budget of the Earth-atmosphere system has been improved substantially with the advent of satellite observations from the Earth Radiation Budget Experiment (ERBE) [see *Barkstrom*, 1984] of the 1980s to the recent Clouds and the Earth's Radiant Energy System (CERES) [see *Wielicki et al.*, 1996, 1998]. The Earth-atmosphere system absorbs ~70% of the solar energy incident at the top of atmosphere (TOA), partly by the surface and partly by the atmospheric column. The absorption of solar energy in the atmosphere plays a key role in the Earth's climate system, not only because it affects the amount of solar energy absorbed by the Earth system, but also because it changes the vertical distribution of absorbed energy, which in turn impacts surface evaporation, atmospheric convection and precipitation. Unfortunately, atmospheric column absorption is an extremely difficult quantity to observe directly. It requires observations of radiation at the surface of the Earth with corresponding matched observations at the top of the atmosphere. The space and time matching of such observations is inherently difficult, especially for cloudy conditions which are highly variable in space and time [e.g., *Stephens and Tsay*, 1990]. Reliable modeling of the atmospheric column absorption requires not only an accurate radiative transfer model, but accurate cloud physical and optical properties as input to the model.

[1]Department of Atmospheric Sciences, University of North Dakota, Grand Forks, North Dakota, USA.
[2]NASA Langley Research Center, Hampton, Virginia, USA.
[3]Department of Meteorology, University of Utah, Salt Lake City, Utah, USA.
[4]Science Systems and Applications Incorporated (SSAI), Hampton, Virginia, USA.


0148-0227/08/2007JD009769$09.00

[3] The difference between observed and model-calculated cloud absorption of solar radiation is referred to as the cloud absorption anomaly (CAA). *Stephens and Tsay* [1990] reviewed and summarized various reasons, such as cloud inhomogeneities and microphysical properties, to explain CAA. CAA became a larger issue with the publication of three articles in 1995 [*Cess et al.*, 1995; *Ramanathan et al.*, 1995; *Pilewskie and Valero*, 1995] which argued that the observed cloud absorption is about 40% larger than the radiative transfer model calculations. *Li et al.* [1999] summarized mechanisms to explain the reported large anomalous absorption, including the effects of inhomogeneous clouds, large cloud droplets, aerosols, water vapor dimers, continuum absorption, and use of inaccurate radiative parameterizations, but they were not able to account for the estimated global averaged CAA of $\sim$25$-$30 $Wm^{-2}$ in the *Cess et al.* [1995] study. To further investigate the CAA, the Department of Energy sponsored the Atmospheric Radiation Measurement [ARM, *Ackerman and Stokes*, 2003] Enhanced Shortwave Experiment (ARESE) at the ARM Southern Great Plains (SGP, 36.61°N, 97.49°W) site during September–October 1994. The initial analyses of a subset of the ARESE data revealed an even larger cloud absorption [*Valero et al.*, 1997; *Zender et al.*, 1997], $\sim$0.37 of the total incoming solar radiation, which could not be explained by current existing radiative transfer theory [*Ackerman et al.*, 2003]. Later analyses of the ARESE data indicated that the overestimated cloud absorption in the *Valero et al.* [1997] and *Zender et al.* [1997] studies might be due to contaminated aircraft data [*Valero et al.*, 2000; *Ackerman et al.*, 2003; *Li et al.*, 1999].

[4] Given the uncertain situation after the ARESE, ARM hosted a second field experiment (ARESE II) at the ARM SGP site during March 2000 to further investigate physical processes of the CAA. *Ackerman et al.* [2003] used more complete surface and aircraft in situ measurements in state-of-the-art radiative transfer model calculations during the ARESE II, concluding that the model-calculated column absorption agreed with observations to within 10% of the total column absorption for both cloudy and cloud-free conditions. This agreement was a factor of 4 closer than found in the 1995 CAA papers. The primary improvements were thought to arise from the elimination of potentially contaminated aircraft data, and inclusion of more accurate treatments of gas absorption in the radiative transfer calculations.

[5] The results derived from both ARESE and ARESE II field experiments, however, are based on low-level overcast stratus clouds with a very limited number of case studies: one case during ARESE and two cloud-free and three cloudy cases during ARESE II. We conclude that it remains key to investigate the CAA in other types of clouds and using larger numbers of cases. The present study uses a new generation of collocated satellite-surface measurements to derive the atmospheric column absorption and evaluates the CAA for thick ice clouds, including deep convection cases. We have collected 5 years of collocated satellite-surface data and compared these observations with state-of-the-art radiative transfer model calculations in the tropics and middle latitudes. For the first time, the statistics of the absorption of solar energy in the atmosphere in the optically thick Deep Convective Systems (DCS) have been thoroughly investigated using both the collocated satellite-surface data and a state-of-the-art radiative transfer model.

[6] There are several reasons to focus such a study on DCS. First, new CERES global observations of the anisotropy of broadband solar reflected radiation have shown that optically thick ice clouds provide the most Lambertian (i.e., uniform radiance in angle) targets for conversion of radiance to flux [*Hu et al.*, 2004]. Therefore the CERES derived Angular Distribution Models [ADMs, *Loeb et al.*, 2003a, 2003b] show the lowest percentage errors for these scene types. Unlike the ERBE TOA flux estimates, the new ADMs can provide radiative fluxes without large biases for extreme cloud types such as produced by deep convection. The ERBE ADMs were based on a simple average of radiances taken in all overcast cloud conditions. The CERES ADMs provide specific ice cloud anisotropy as a function of optical depth for both broken and overcast conditions. Only the simpler overcast conditions are considered here. A second major advantage of DCS is that for high altitude overcast ice clouds, water vapor levels are low, and solar absorption has little dependence on water vapor amounts above, within, or below the cloud. A third advantage is the use of optically thick clouds. In the optically thick limit, ice cloud particle habit and phase function differences are greatly reduced by the multiple scattering field. Particle habit uncertainty would be much more important for optically thin ice clouds. Optically thick overcast clouds also reduce the variability in surface flux observations at the ARM sites. In the optically thick limit (e.g., visible optical depths > 80) surface solar radiation tends to zero, and TOA albedo becomes relatively insensitive to cloud optical depth. Finally, the use of extensive high ice cloud systems (overcast 100 km regions) greatly reduces the ability of 3-D cloud effects to horizontally transport solar energy out of the region considered for atmospheric column absorption. The ice clouds used in this study are topped by large high altitude anvils, or are extensive midlatitude storm systems with ice cloud dominating at altitudes >5 km.

[7] In this study we will use combined satellite-surface observations of the atmospheric column to explore two primary questions:

[8] (1) How well do these collocated satellite-surface observations agree quantitatively with the radiative transfer model calculations in the optically thick limit for TOA albedo, surface absorption, and atmospheric column absorption?

[9] (2) What are the similarities and differences of the radiation budgets of DCS between the tropics and the middle latitudes?

## 2. Data

[10] Satellite and surface shortwave (SW) observations were collected from March 2000 through December 2004 when the NASA Terra satellite ($\sim$10:30 am local time) flew over the ARM TWP sites (Manus: 2.06°S, 147.43°E; Nauru: 0.52°S, 166.92°E) and SGP site, and from July 2002 to December 2004 for the NASA Aqua satellite ($\sim$1:30 pm local time). Since there are significant spatial and temporal differences between surface and satellite observations, such as the small surface field of view compared to the $\sim$20-km satellite field of view, the temporal and spatial scales should be matched as closely as possible.

The surface data were averaged over a 2-h interval centered at the time of the satellite overpass, and the satellite data were averaged within a $1^\circ \times 1^\circ$ area centered on the ARM sites. *Cess et al.* [1996] made a considerable effort to understand the field-of-view differences between satellite and surface measurements. They used the averaged flux of a network of 11 surface pyranometers located within $\sim 0.8^\circ \times 0.8^\circ$ region as a reference, then compared the reference with the 1-min, 20-min, 40-min, and 60-min averages measured by a single surface station, and obtained the closest agreement using a 60-min average. Note that for ice cloud upper level winds of 15 m/s, the two hour averaging interval used in this study is equivalent to a frozen turbulence spatial scale of 108 km.

[11] Surface inhomogeneity is another important factor to be investigated. The ARM SGP site has a relatively homogeneous geography, its clear-sky SW albedo near the central facility is ~0.17 at local noon [*Minnis et al.*, 1995a]. The western and eastern sides of the central facility are slightly drier and wetter, respectively, than the central facility resulting in 1–2% higher and lower surface albedos than the central facility. The comparison of surface albedos for $0.3^\circ$ and $2.5^\circ$ regions centered on the central facility shows very good agreement by *Minnis et al.* [1995a]. As a result, the surface measured SW albedo at the SGP site is used in this study. For the TWP sites, it is much more complicated because the surface upward SW fluxes were measured on small islands surrounded by ocean. The ARM TWP C2 site is located at Nauru Island, the Republic of Nauru. The island is relatively small (a few kilometers) and its effect on the radiation budget of a 1-degree region can be ignored. The ARM TWP C1 site at Manus Island is slightly larger than Nauru Island. The percentage of Manus area relative to the $1^\circ$ grid box is 11% averaged over all the Terra and Aqua overpasses. Thus the averaged surface albedo of the $1^\circ$ grid box that affects the TOA albedo is the sum of the ARM-measured surface albedo weighted by the percentage of Manus area relative to the $1^\circ$ box and diffuse ocean albedo weighted by ocean percentage. The ocean albedo is calculated using the coupled ocean-atmosphere radiative transfer model, provided by Drs. Zhonghai Jin and Thomas Charlock at NASA Langley, which accounts for atmosphere, aerosols, waves, wind speed (http://sundog.larc.gov/jin/rtset.html) [*Jin et al.*, 2004, 2006]. Note that in all cases, the surface albedo will be insignificant for radiation budget calculations for $\tau > 20$.

[12] The satellite data sets used in this study are the Terra Edition2B and Aqua Edition1B CERES Single Scanner Footprint (SSF) products and include the "Rev1" calibration adjustment to the CERES SW record [*Matthews et al.*, 2005] to account for optics contamination during the first few years on orbit. While the adjustment is small (1 to 2%) it is necessary for the level of accuracy desired in the present comparison. The CERES SSF product combines the CERES broadband fluxes with coincident cloud retrievals using the Moderate Resolution Imaging Spectroradiometer (MODIS) imager. The CERES instruments on the *Terra* and *Aqua* satellites measure radiances that are converted to broadband fluxes using ADMs sampled and optimized for each satellite orbit. Estimated uncertainties in the solar-reflected ($SW^{\uparrow}_{toa}$) and Earth-emitted ($LW^{\uparrow}_{toa}$) single field-of-view instantaneous radiative fluxes at TOA are 13 $Wm^{-2}$ and 4.3 $Wm^{-2}$, respectively [*Chambers et al.*, 2002; *Loeb et al.*, 2003a, 2003b] for all-sky conditions and somewhat less for clear-sky cases. CERES also developed a set of algorithms to derive cloud phase, effective cloud height ($H_e$) and temperature ($T_e$), water-droplet effective radius ($r_e$) or ice-crystal effective diameter ($D_e$), optical depth ($\tau$), and liquid water path (*LWP*) or ice water path (*IWP*) for each imager pixel (1 km resolution, sampled every 2 km) if it has been classified as cloudy by the CERES cloud mask [*Minnis et al.*, 1995b, 2004]. The effective particle sizes are retrieved based on the reflectance at 3.8-$\mu$m. For clouds above 500 hPa, the primary technique for determining $H_e$ is to first estimate $T_e$ from the infrared (IR, 10.8 $\mu$m) radiance, and then determine $H_e$ as the lowest altitude having $T_e$ in a vertical profile of atmospheric temperature from the reanalyses provided by the Global Modeling Assimilation Office GEOS 4.03 [*Bloom et al.*, 2005]. These cloud properties are hereafter referred to as CERES-MODIS cloud properties.

[13] The surface data set (5-min resolution) is either collected directly or derived from surface measurements. The surface up- and down-looking standard Eppley Precision Spectral Pyranometers (PSPs) provide measurements of downwelling ($SW^{\downarrow}_{sfc}$) and upwelling ($SW^{\uparrow}_{sfc}$) broadband SW (0.3 to 3 $\mu$m) fluxes at the surface. The SW fluxes are the Best Estimate Flux Value Added Products (VAP) of the ARM program, and their uncertainties are ~10 $Wm^{-2}$ [*Shi and Long*, 2002]. Cloud top height ($H_{top}$) is derived from cloud radar reflectivity profiles with an uncertainty of 90 m. Cloud base height ($H_{base}$) is derived from a composite of Belfort laser ceilometer, micropluse lidar, and cloud radar data [*Clothiaux et al.*, 2000]. The cloud *LWP* is derived from the microwave radiometer brightness temperatures measured at 23.8 and 31.4 GHz using a statistical retrieval method [*Liljegren et al.*, 2001].

## 3. Radiation Budgets at the TWP and SGP Sites

[14] Four kinds of SW fluxes are used to study the DCS radiation budgets; they are downwelling ($SW^{\downarrow}_{sfc}$) and upwelling ($SW^{\uparrow}_{sfc}$) broadband SW fluxes at the surface, and downwelling ($SW^{\downarrow}_{toa}$) and upwelling ($SW^{\uparrow}_{toa}$) broadband SW fluxes at TOA, respectively. The $SW^{\downarrow}_{toa}$ is calculated by

$$SW^{\downarrow}_{toa} = 1365 * \mu_0 / (d/d_m)^2, \tag{1}$$

where 1365 $Wm^{-2}$ is the Total Solar Irradiance at the annual average Sun-Earth distance, $\mu_0$ is the cosine of solar zenith angle, and the $d$ and $d_m$ are the actual and mean Sun-Earth distances, respectively. The ratio of $d$ to $d_m$ never departs from unity by more than 3.5%, and ranges from 0.9668 (closest to the Sun) to 1.0337 (farthest from the Sun). The TOA albedo ($R_{toa}$), Earth-atmosphere system absorption ($A_{sys}$), surface absorption ($A_{sfc}$), and atmospheric column absorption ($A_{col}$) can be calculated, respectively, as

$$\begin{aligned} R_{toa} &= SW^{\uparrow}_{toa} / SW^{\downarrow}_{toa}, \\ A_{sys} &= 1 - R_{toa}, \\ A_{sfc} &= \left( SW^{\downarrow}_{sfc} - SW^{\uparrow}_{sfc} \right) / SW^{\downarrow}_{toa}, \\ A_{col} &= A_{sys} - A_{sfc}. \end{aligned} \tag{2}$$

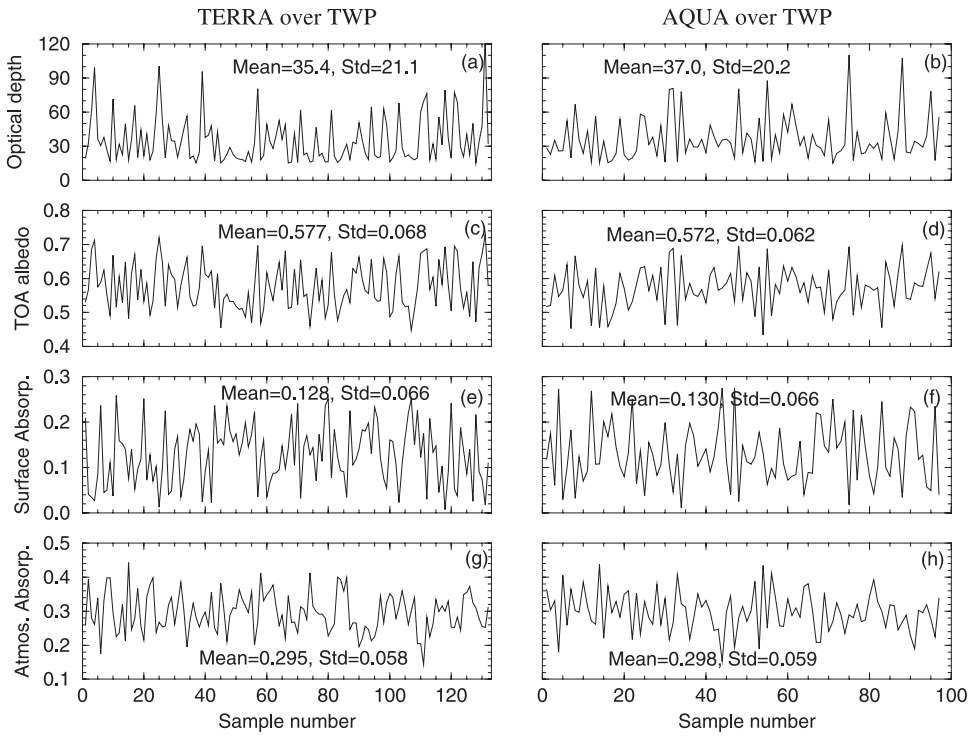


**Figure 1.** Left column includes the CERES-MODIS-derived (a) cloud optical depth, (c) CERES-derived TOA albedo, (e) ARM-measured surface absorption, and (g) estimated column absorption ($A_{col} = 1 - R_{toa} - A_{sfc}$) for *Terra* overpass the TWP sites from March 2000 to December 2004. Right column (b, d, f, h) is for *Aqua* overpass the TWP sites from July 2002 to December 2004.

[15] The criteria for selecting the DCS cases are (1) the 1° averaged (logarithmic) cloud optical depth is larger than 15, (2) surface absorption is less than 0.3, (3) cloud top or effective cloud height exceeds 5 km, and (4) the averaged cloud fraction from the CERES SSF product within a 1° × 1° box centered at the ARM sites is greater than 99%. A total of 132 and 97 DCS cases were observed by *Terra* and *Aqua*, respectively, at the ARM TWP sites. At the ARM SGP site, *Terra* and *Aqua* detected a total of 116 and 66, respectively.

[16] Figure 1 shows the 1° × 1° averages of the CERES-derived $\tau$ and $R_{toa}$, the 2-hr averages of the ARM-measured $A_{sfc}$, and the estimated $A_{col}$ values when Terra and Aqua passed over the ARM TWP sites. Their corresponding Probability Distribution Functions (PDF) and Cumulative Distribution Functions (CDF), based on the 132 *Terra* and 97 *Aqua* cases at the ARM TWP sites, are plotted in Figure 2. As demonstrated in Figures 1 and 2, the averaged *Terra* and *Aqua* cloud-radiation properties at the TWP sites are nearly identical, and their median and mode values are close to their corresponding mean values (nearly normal distributions) except for cloud optical depth, which has a long tail toward to higher values. The cloud-radiation properties of *Terra* and *Aqua* at the ARM SGP site have slight differences (up to 1.5%, Figure 3), and their corresponding PDFs and CDFs (Figure 4) are very similar to those at the TWP sites.

[17] Table 1 lists the averaged cloud property and radiative flux observations, including cloud height and temperature, *LWP*, $D_e$, and SW fluxes from the *Terra* and *Aqua* cases at both sites. The $H_{base}$ values are almost the same (∼1 km) at both sites, but the SGP $H_{top}$ values (∼9 km) are about 1 km lower than those at the TWP (∼10 km) due to a shallower midlatitude troposphere compared to that in the deep tropics. The MODIS-derived $H_e$ values are ∼1.4 km lower than the ARM radar-derived $H_{top}$ at the SGP site, but are 2.6 km higher than $H_{top}$ at the TWP sites. The DOE ARM 35 GHz cloud radar has minimum-detectable reflective factors (Z) of −55 dBZ at 1 km and −35 dBZ at 10 km [*Moran et al.*, 1998]. While the cloud radar signals might be attenuated at the uppermost DCS layers, especially during summer and autumn seasons at the SGP site, this effect is thought to be small given the moderate LWP values shown in Table 1. At the TWP sites, however, many of the DCS upper layers may be missed due to strong attenuation by the large *LWP* values, thus keeping the radar signals from penetrating through to the cloud top. This effect is thought to explain the much colder and higher altitude satellite observed ice cloud $T_e$ and $H_e$. The opposite occurs at the SGP, where the satellite thermal emission temperature and equivalent height is expected to be below the radar cloud top height when radar attenuation is not an issue [*Sherwood et al.*, 2004]. For the cases in this analysis, the MODIS-derived $T_e$ values at the TWP sites are about 24 K colder, and $D_e$ values are 14 $\mu$m larger, than those at the SGP site.

[18] The seasonal and annual averages and 95% confidence intervals listed in Tables 2 and 3 provide the statistics of all selected *Terra* and *Aqua* cases within a 3-month season at the TWP and SGP sites, respectively. The four seasons are defined here as winter from December to February (DJF), spring from March to May (MAM), summer from June to August (JJA), and autumn from September to

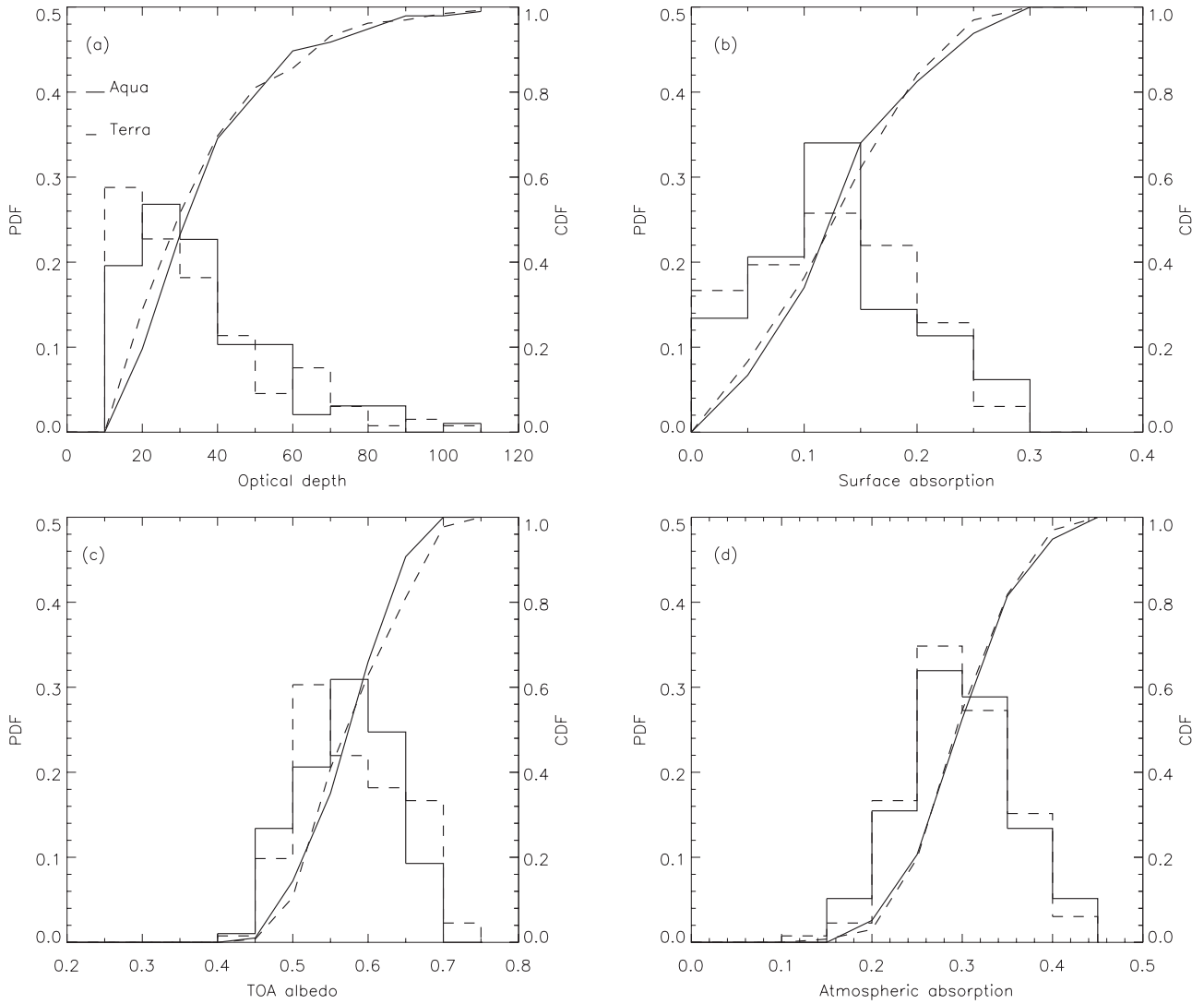


**Figure 2.** Probability Distribution Functions (PDF) and Cumulative Distribution Functions (CDF) of 132 *Terra* cases (dashed line) and 97 *Aqua* cases (solid line) at the ARM TWP sites for (a) optical depth, (b) surface absorption, (c) TOA albedo, and (d) atmospheric absorption.

November (SON). There are no strong seasonal variations of cloud-radiation properties (<8% of the annual averages) at the TWP sites, but there are significant seasonal variations (up to 61% of the annual averages) at the SGP site. The SGP differences are dominated by seasonal variations in solar insolation, as well as a varying seasonal mix of deep convective ice clouds versus baroclinic storm thick ice clouds. Consistent with this interpretation, the effective cloud height at the SGP is higher by about 2 km in the summer months.

[19] Each parameter in Tables 2 and 3 includes 95% confidence bounds for the mean value given in the tables, assuming each satellite overpass is independent. The mean fluxes are used with equation (2) to determine the $R_{toa}$, $A_{sfc}$, and $A_{col}$ values. $R_{toa}$ is extremely stable for the TWP cases in all seasons, with a range of less than 0.01, a mean of 0.575, and 95% confidence bound on the mean value of only 0.008. $A_{sfc}$ and $A_{col}$ average 0.129 and 0.296, respectively, both with 95% confidence bounds of less than 0.01. The equivalent values at the SGP show 6 times as much seasonal variability in $R_{toa}$, but the annual average values of $R_{toa}$, $A_{sfc}$, and $A_{col}$ are within 0.01 to 0.02 of the TWP values. The $A_{col}$ values of 0.285 for SGP and 0.296 for TWP are larger than expected [e.g., *Ackerman et al.*, 2003], so further analyses of the results are shown in Tables 4 and 5 below, in particular how the results change as the restriction on overcast ice cloud optical depth is increased. As optical thickness increases for overcast extensive cloud layers, we expect spatial variability for both the satellite and surface site to be reduced. The reason is that in the very large optical depth limit, albedo is expected to saturate to near 0.8, and surface absorption to near zero. However, are there enough cases at these high optical depths for a rigorous analysis?

[20] Tables 4 and 5 list the averages of all $R_{toa}$, $A_{sfc}$, $A_{col}$, and $\tau$ presented in Figures 1 and 3, at the TWP and SGP sites, respectively. With increased $\tau$, $R_{toa}$ increases, and both $A_{sfc}$ and $A_{col}$ decrease. When $\tau$ is greater than 50, however, $A_{col}$ is nearly constant at both sites, indicating that $A_{col}$ is saturated and tends to have the same value in the tropics and middle latitudes in the optically thick limit. Surface albedo has

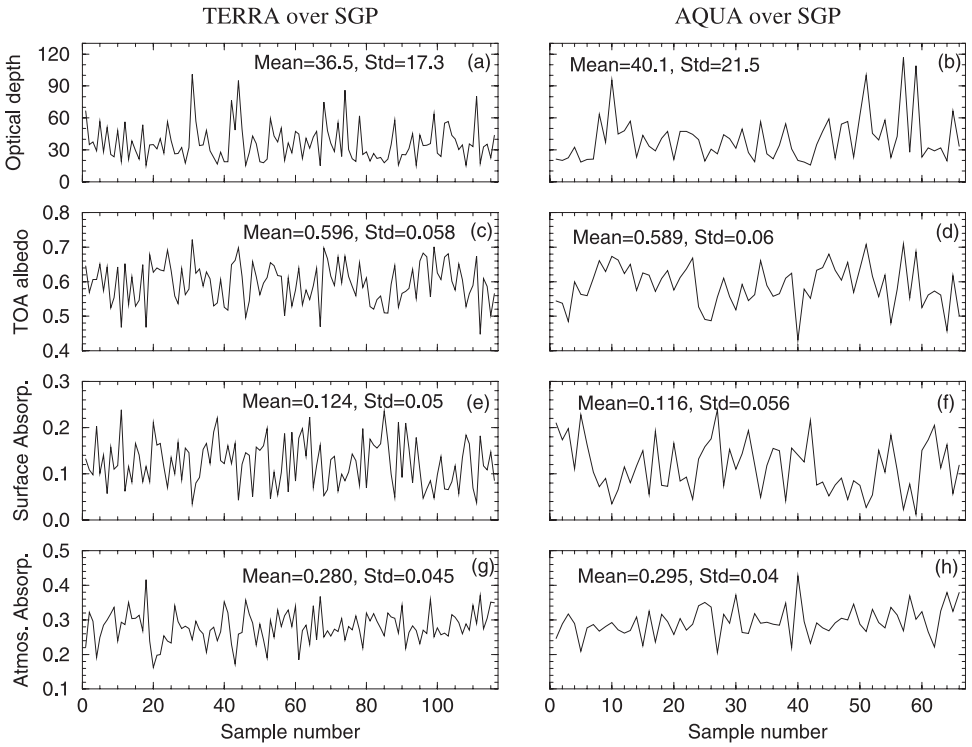


**Figure 3.** Same as Figure 1, except for *Terra* overpasses of the ARM SGP site from March 2000 to July 2004, and for *Aqua* overpasses of the ARM SGP site from July 2002 to July 2004.

minimal influence on the radiation budget in the optically thick limit, but it is important for cases with lower optical depths. However, what about the variability of these optically thicker cases? The variability has reduced so dramatically that the 95% confidence bound on $A_{col}$ for just 10 TWP cases with $\tau > 80$ is 0.009, about the same value as for 229 cases with $\tau > 15$. Tables 4 and 5 also demonstrate clearly that as the selected optical depth increases, $A_{col}$ systematically reduces and asymptotes to a value of $0.265 \pm 0.01$ for the thick ice cloud cases, both for TWP and for SGP.

[21] The escape of solar photons through the sides of horizontally finite DCS is a potential problem in calculating $A_{col}$ because the "solar photon leaks" through the sides of DCS are incorrectly interpreted as absorption within the DCS, and would tend to overestimate $A_{col}$ [*Stephens and Tsay*, 1990]. *Stephens and Tsay* [1990] found that there are almost no solar photon leaks if the DCS diameters are greater than 60 km, i.e., as the horizontal extent of DCS systematically increases to 60 km, the inferred $A_{col}$ converges to the plane parallel value. Most DCS diameters range from 200 to 400 km in the tropics [*Lin et al.*, 2006], but the horizontal dimension of a DCS is maximum when viewed from space and is dominated by the mesoscale outflow region (when anvils are optically thick). The convective cores may be narrower, and some photon leakage may take place there. However, if most of the scattering and absorption takes place in the upper few kilometers of the DCS, the lower altitude towers may play a relatively minor role. In addition, the spatial average of $1^\circ \times 1^\circ$ satellite data used in this study should be large enough to minimize the effect of horizontal leakage of photons. Although there is no record of their effective sizes in the middle latitudes, the midlatitude DCSs are likely larger than 60 km. The 100-km scale of the 1-degree analysis regions used in this study should act to select horizontally extensive cloud systems.

## 4. Comparison With Radiative Transfer Model Calculations

[22] To compare the model calculations with observations, the NASA Langley Fu-Liou Proto-Edition 3 code [*Rose et al.*, 2006] is used to calculate the DCS radiation budgets. The NASA Langley modified Fu-Liou radiative transfer model is the gamma-weighted two-stream approximation with the inputs of linear and logarithmic averages of cloud optical depth to account for cloud horizontal inhomogeneity [*Kato et al.*, 2005]. The average error in the TOA irradiance caused by the gamma-weighted two-stream approximation is 6.1 $Wm^{-2}$ ($\sim$0.005 albedo bias) at 30° solar zenith angle under one-layer overcast conditions [*Kato et al.*, 2005]. The original Fu-Liou 6 broad SW bands have been expanded into 18 to improve the treatment of Rayleigh scattering, aerosols, and ozone, as well as to better understand the higher spectral resolution of ice absorption in 0.69–1.9 $\mu$m near-IR region [*Rose et al.*, 2006]. The new version of Fu-Liou code has higher TOA albedos ($\sim$3%) and less ($\sim$3%) cloud absorption than the older version under optically thick ice cloud conditions ($\tau > 80$). *Rose et al.* [2006] used more than 5 years of collocated satellite-surface SW observations over 48 surface sites to validate the calculations of the Proto-Edition 3 code and concluded that the mean differences (model calculations minus observations) are 5.4 $Wm^{-2}$ for TOA reflected SW flux and

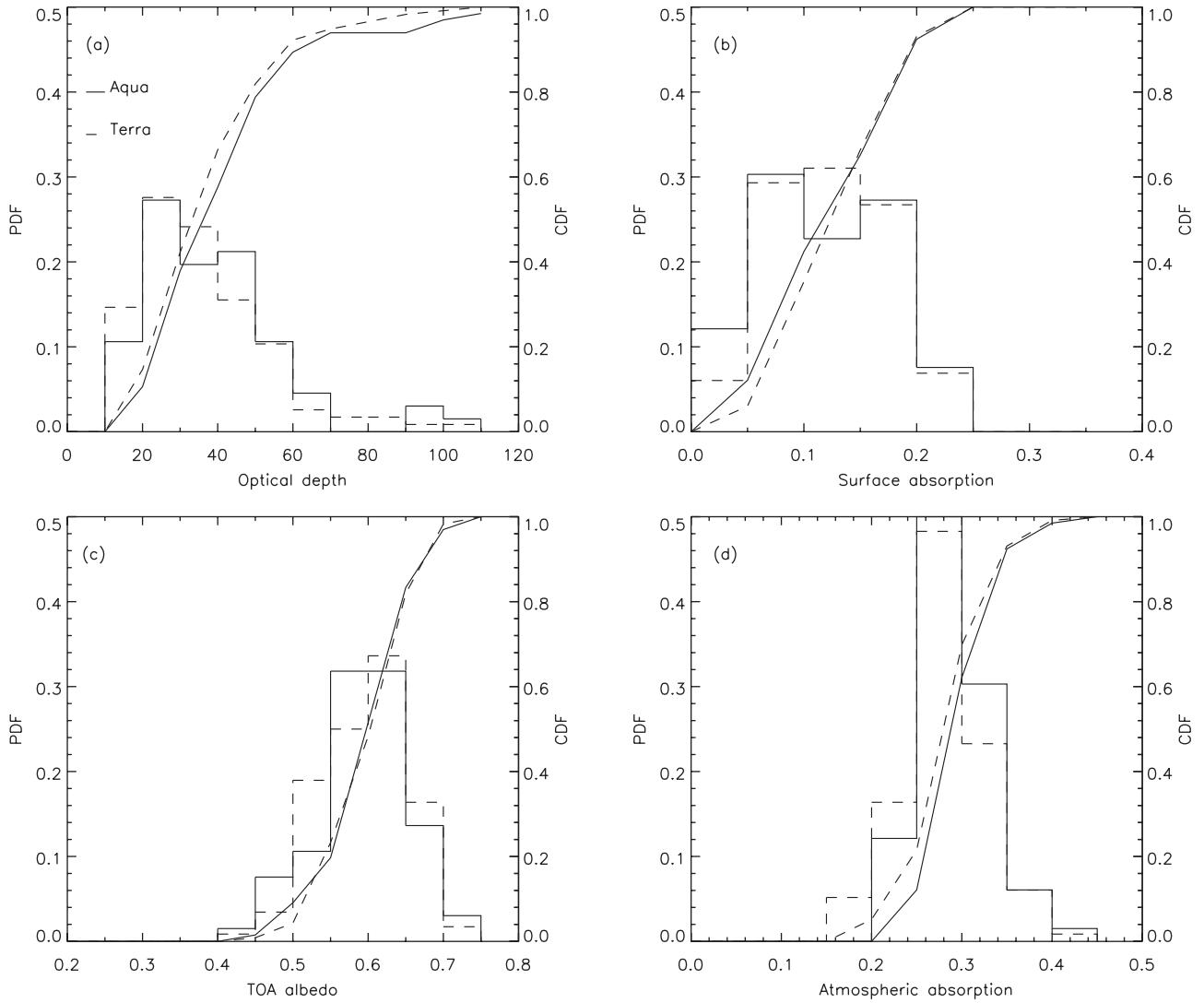


**Figure 4.** Probability Distribution Functions (PDF) and Cumulative Distribution Functions (CDF) of 116 *Terra* cases (dashed line) and 66 *Aqua* cases (solid line) at the ARM SGP site for (a) optical depth, (b) surface absorption, (c) TOA albedo, and (d) atmospheric absorption.

9.7 $Wm^{-2}$ for downward SW transmission at the surface. The TOA albedo calculated by the Proto-Edition 3 code also compares with a high spectral resolution and angular resolution DISORT benchmark calculation, and the mean difference is ~0.5% for DCS. Furthermore, the mean TOA albedo in Figure 5, calculated by the Proto-Edition 3 code, is exactly the same as the results of the *Hu et al.* [2004] DISORT calculation with the inputs of $D_e = 80$ $\mu$m

**Table 1.** Mean Values of *Terra* and *Aqua* Cloud-Radiation Properties at the Both TWP and SGP Sites

| | TWP | | SGP | | |
|---|---|---|---|---|---|
| Parameters | Terra | Aqua | Terra | Aqua | Data Source |
| $H_{base}$, km | 1.011 | 1.017 | 1.116 | 1.042 | ARM lidar |
| $H_{top}$, km | 10.01 | 9.585 | 9.034 | 8.890 | Radar radar |
| $\Delta H$, km | 9.0 | 8.568 | 7.917 | 7.848 | ARM lidar And radar |
| $H_e$, km | 12.368 | 12.480 | 7.473 | 7.726 | CERES SSF |
| $T_e$, K | 226.9 | 224.4 | 248.3 | 251.7 | CERES SSF |
| $D_e$, $\mu$m | 67.4 | 65.1 | 52.3 | 52.5 | CERES SSF |
| LWP, $gm^{-2}$ | 5245 | 4403 | 744 | 1154 | ARM microwave |
| $SW^{\downarrow}_{sfc}$, $Wm^{-2}$ | 169.4 | 168.2 | 152.6 | 143.3 | ARM pyranometer |
| $SW^{\uparrow}_{sfc}$, $Wm^{-2}$ | 30.1 | 29.7 | 27.0 | 26.0 | ARM pyranometer |
| $SW^{\downarrow}_{toa}$, $Wm^{-2}$ | 1209.5 | 1201.5 | 997.5 | 994.8 | calculated by equation (1) |
| $SW^{\uparrow}_{toa}$, $Wm^{-2}$ | 697.3 | 687.3 | 590.8 | 582.5 | CERES SSF |

**Table 2.** Seasonal and Annual Averages and 95% Confidence Intervals of Cloud-Radiation Properties at the ARM TWP Sites

| | Winter | Spring | Summer | Autumn | Annual | |
|---|---|---|---|---|---|---|
| Parameter/# of Sample | N = 55 | N = 42 | N = 67 | N = 65 | N = 229 | Data Source |
| $H_e$, km | 12.35 (±0.37) | 12.53 (±0.35) | 12.32 (±0.31) | 12.50 (±0.28) | 12.42 (±0.16) | CERES SSF |
| $T_e$, K | 226.5 (±4.63) | 226.0 (±4.50) | 226.3 (±3.93) | 224.7 (±3.49) | 225.8 (±2.04) | CERES SSF |
| $D_e$, $\mu$m | 61.1 (±3.12) | 68.4 (±3.45) | 67.6 (±2.20) | 67.7 (±2.71) | 66.3 (±1.44) | CERES SSF |
| Optical depth | 34.7 (±5.27) | 35.3 (±6.39) | 37.2 (±5.25) | 36.4 (±4.94) | 36.0 (±2.69) | CERES SSF |
| LWP, g m$^{-2}$ | 5078 (±1184) | 6028 (±1853) | 4714 (±1041) | 4971 (±1095) | 5112 (±618) | ARM microwave |
| $R_{sfc}$ | 0.067 (±0.004) | 0.080 (±0.004) | 0.077 (±0.004) | 0.078 (±0.004) | 0.078 (±0.002) | ARM, $SW^{\uparrow}_{sfc}/SW^{\downarrow}_{sfc}$ |
| $R_{toa}$ | 0.573 (±0.018) | 0.568 (±0.021) | 0.578 (±0.016) | 0.578 (±0.014) | 0.575 (±0.008) | CERES, $SW^{\uparrow}_{toa}/SW^{\downarrow}_{toa}$ |
| $A_{sfc}$ | 0.130 (±0.016) | 0.125 (±0.020) | 0.135 (±0.016) | 0.124 (±0.017) | 0.129 (±0.009) | $(SW^{\downarrow}_{sfc}-SW^{\downarrow}_{sfc})/SW^{\downarrow}_{toa}$ |
| $A_{col}$ | 0.297 (±0.017) | 0.307 (±0.017) | 0.287 (±0.014) | 0.298 (±0.013) | 0.296 (±0.007) | $1-R_{toa}-A_{sfc}$ |
| $SW^{\downarrow}_{sfc}$, W m$^{-2}$ | 174.6 (±21.6) | 168.4 (±27.9) | 167.2 (±20.8) | 165.9 (±22.6) | 168.8 (±11.4) | ARM pyranometer |
| $SW^{\uparrow}_{sfc}$, W m$^{-2}$ | 30.6 (±4.1) | 29.8 (±5.4) | 30.0 (±4.0) | 29.2 (±4.3) | 29.9 (±2.2) | ARM pyranometer |
| $SW^{\downarrow}_{toa}$, W m$^{-2}$ | 1233.8 (±13.7) | 1233.5 (±21.3) | 1141.7 (±16.2) | 1231.4 (±14.4) | 1206.1 (±9.7) | calculated by equation (1) |
| $SW^{\uparrow}_{toa}$, W m$^{-2}$ | 706.0 (±21.7) | 700.8 (±28.4) | 658.8 (±18.4) | 712.2 (±19.4) | 693.0 (±11.0) | CERES SSF |

and $\mu_0 = 0.9$. Therefore we are confident in using the newly developed Fu-Liou code to calculate the radiative fluxes used in this study.

[23] From the comparison, we want to quantitatively study how well the state-of-the-art radiative transfer model calculations agree with the collocated satellite-surface observations in the optically thick limit. Given the increased uniformity of the high optical depth cases apparent in Tables 4 and 5, we seek to further improve the space-time matching for these cases. The surface observations are averaged over a 0.5-h interval and the satellite results are averaged over a 20-km × 20-km box centered on the ARM TWP sites during the comparison. The 12 cases have been re-selected from the original 229 *Terra* and *Aqua* cases at the TWP sites with the following criteria: (1) $\tau > 80$, (2) homogeneity factor, $(\tau_{mean}/\tau_{std})^2 > 10$, and (3) the ratio of standard deviation to mean $A_{sfc}$ is less than 25%. The first criterion is used because clouds and $A_{sfc}$ have become relatively insensitive to optical depth, which should be the best balance of maximizing cases (reduced noise in $R_{toa}$) versus reducing noise ($A_{sfc}$). The last two criteria are designed to find the most space and time uniform systems. We concentrate on the TWP site for the comparison study because as shown in Tables 4 and 5 there are more samples and they showed the least dependence on seasonal cycle along with the lowest 95% confidence bounds even for small numbers of cases. To obtain a better vertical profile of cloud particle size for the calculations, it is desirable to have $D_e$ retrievals at near-infrared wavelengths, such as 2.1 $\mu$m. Those values correspond to a greater depth in the cloud. Since there are no 2.1-$\mu$m $D_e$ retrievals in the current CERES SSF products, a special effort was to retrieve ice cloud particle size at $\lambda$ = 2.1 $\mu$m for the re-selected 12 cases. Reflectance lookup tables for radiances at 2.1 $\mu$m were created for the same ice cloud models used [*Minnis et al.*, 1998] in the CERES-MODIS retrievals. These were used along with a simple radiative transfer parameterization to retrieve $D_e$ values in a manner consistent with the standard CERES cloud analysis.

[24] We performed a variety of model calculations both to show which cloud parameters are dominant and to explore common assumptions, such as single uniform cloud layers in the vertical. For all model calculations, the observed $H_e$ and $\tau$ values were used in the model for each case. All calculations also used $\tau_{aerosol} = 0.2$, $H_{base} = 1$ km, and a standard tropical sounding. We then performed six model calculations; their results are shown in Figure 5.

[25] The first type of calculation uses a simple vertically uniform single cloud layer with $D_e$ equal to 60 $\mu$m (FL60), 100 $\mu$m (FL100), and 140 $\mu$m (FL140). The second type (FL37 and FL21) includes each individual $R_{sfc}$, $\mu_0$, layer-mean $D_{e37}$ values (retrieved at $\lambda$ = 3.7 $\mu$m) and $D_{e21}$ values (retrieved at $\lambda$ = 2.1 $\mu$m) for the 12 selected DCS cases.

[26] The third type (FL_P) is the same as the second except that it varies the vertical profiles of $D_e$ and $\tau$ (10 sublayers).

**Table 3.** Seasonal and Annual Averages and 95% Confidence Intervals of Cloud-Radiation Properties at the ARM SGP Site

| | Winter | Spring | Summer | Autumn | Annual | |
|---|---|---|---|---|---|---|
| Parameter/# of Sample | N = 43 | N = 64 | N = 27 | N = 48 | N = 182 | Data Source |
| $H_e$, km | 7.20 (±0.74) | 7.50 (±0.71) | 8.99 (±0.92) | 7.18 (±0.69) | 7.57 (±0.39) | CERES SSF |
| $T_e$, K | 245.2 (±4.54) | 248.5 (±5.20) | 252.2 (±7.91) | 253.2 (±5.64) | 249.5 (±2.98) | CERES SSF |
| De, $\mu$m | 55.5 (±5.52) | 49.1 (±5.52) | 45.9 (±5.52) | 57.1(±5.52) | 52.2 (±5.52) | CERES SSF |
| Optical depth | 39.5 (±5.48) | 38.9 (±4.56) | 38.6 (±8.85) | 34.4 (±4.87) | 37.8 (±2.75) | CERES SSF |
| LWP, g m$^{-2}$ | 600 (±202) | 718 (±234) | 1154 (±583) | 1560 (±608) | 969 (±209) | ARM microwave |
| $R_{sfc}$ | 0.163 (±0.010) | 0.175 (±0.007) | 0.187 (±0.008) | 0.158 (±0.008) | 0.169 (±0.004) | ARM, $SW^{\uparrow}_{sfc}/SW^{\downarrow}_{sfc}$ |
| $R_{toa}$ | 0.624 (±0.013) | 0.588 (±0.014) | 0.563 (±0.023) | 0.592 (±0.017) | 0.594 (±0.008) | CERES, $SW^{\uparrow}_{toa}/SW^{\downarrow}_{toa}$ |
| $A_{sfc}$ | 0.100 (±0.013) | 0.126 (±0.013) | 0.132 (±0.021) | 0.127 (±0.015) | 0.121 (±0.008) | $(SW^{\downarrow}_{sfc}-SW^{\downarrow}_{sfc})/SW^{\downarrow}_{toa}$ |
| $A_{col}$ | 0.276 (±0.010) | 0.286 (±0.011) | 0.305 (±0.017) | 0.281 (±0.015) | 0.285 (±0.006) | $1-R_{toa}-A_{sfc}$ |
| $SW^{\downarrow}_{sfc}$, W m$^{-2}$ | 92.8 (±12.8) | 177.0 (±19.8) | 201.2 (±31.5) | 133.4 (±17.5) | 149.2 (±11.4) | ARM pyranometer |
| $SW^{\uparrow}_{sfc}$, W m$^{-2}$ | 15.8 (±2.6) | 32.3 (±4.1) | 38.3 (±6.5) | 22.3 (±3.6) | 26.6 (±2.4) | ARM pyranometer |
| $SW^{\downarrow}_{toa}$, W m$^{-2}$ | 773.8 (±33.1) | 1135.6 (±23.4) | 1236.6 (±14.7) | 875.6 (±35.3) | 996.5 (±29.6) | calculated by equation (1) |
| $SW^{\uparrow}_{toa}$, W m$^{-2}$ | 482.2 (±21.7) | 665.7 (±17.2) | 697.0 (±31.3) | 517.0 (±22.7) | 587.8 (±16.8) | CERES SSF |

**Table 4.** Sensitivity of Cloud-Radiation Properties on $\tau$ at the TWP Sites (Averages and 95% Confidence Intervals)

| Samples (Terra and Aqua) | $\tau$ | $R_{TOA}$ | $A_{sfc}$ | $A_{COL}$ |
|---|---|---|---|---|
| 229 for $\tau > 15$ | 36 (±2.6) | 0.575 (± 0.008) | 0.129 (±0.009) | 0.296 (±0.007) |
| 119 for $\tau > 30$ | 50 (±3.4) | 0.627 (± 0.008) | 0.093 (± 0.010) | 0.280 (± 0.009) |
| 70 for $\tau > 40$ | 61 (±4.2) | 0.650 (± 0.008) | 0.075 (± 0.010) | 0.275 (± 0.010) |
| 45 for $\tau > 50$ | 70 (±5.0) | 0.667 (± 0.008) | 0.070 (± 0.014) | 0.263 (± 0.011) |
| 29 for $\tau > 60$ | 78 (±6.1) | 0.682 (± 0.008) | 0.051 (± 0.015) | 0.267 (± 0.014) |
| 17 for $\tau > 70$ | 88 (±7.7) | 0.693 (± 0.008) | 0.035 (± 0.012) | 0.272 (± 0.012) |
| 10 for $\tau > 80$ | 96 (±10.7) | 0.702 (± 0.010) | 0.030 (± 0.011) | 0.268 (± 0.009) |

(M. Deng and G. G. Mace, Cirrus microphysical properties and air motion statistics using cloud radar doppler moments. Part II: Mid-latitude and tropics comparison and model applications, manuscript in preparation, 2008) used the ARM cloud radar and other observations to retrieve the profiles of cirrus cloud microphysical properties at the ARM TWP sites from June 1999 to July 2000. They found that the averaged cloud-crystal effective diameter ($D_e$) and ice water content (*IWC*) are approximately 90 $\mu$m and 2.5 mg/m$^3$ at the cloud top, and then linearly increase to the cloud center and remain nearly constant at 120 $\mu$m (the ratio $\sim$ 1.3–1.4) and 20 mg/m$^3$ (the ratio $\sim$8) to the bottom of the cloud. Since the CERES-retrieved $D_{e37}$ is representative of cloud particle size near the cloud top (at $\tau_{vis} \approx 3$ down into the cloud from the cloud top as shown in Figure 6), the product of the ARM-derived $D_e$ vertical ratio and CERES-retrieved $D_{e37}$ is input into the model. Also the $\tau$ profile is input into the model where the $\tau$ profile [based on $\tau(z) \sim IWC(z) * \Delta Z/D_e(z)$] is derived using both the ARM-derived *IWC* and $D_e$ profiles to weight the CERES-derived total $\tau$. Thus the $\tau$ values for each layer are dominated by the *IWC* vertical distribution, which increases from the cloud top to the bottom.

[27] Figure 5 shows the comparison of cloud-radiation parameters between the observations and model calculations from the 12 selected cases. The averages (blue diamond) of observed $\tau$, $D_{e37}$, $D_{e21}$, $R_{toa}$, $A_{sfc}$ and $A_{col}$ are 103, 65.8 $\mu$m, 103.9 $\mu$m, 0.706, 0.032, and 0.262, respectively. The mean ratio of $D_{e21}$ to $D_{e31}$ is 1.58, which indicates that the 2.1-$\mu$m retrieved ice particle sizes are much larger and deeper into the clouds (as shown in Figure 6) than those from the 3.7-$\mu$m channel. With fixed $D_e = 100$ $\mu$m (FL100 in Figure 5), the model-calculated $R_{toa}$, $A_{sfc}$, and $A_{col}$ values agree to within 0.01 with the observations. The $D_e$ = 100 $\mu$m is representative of a layer-mean value because it is closer to the mean $D_{e21}$. When $D_e$ increases from 60 to 140 $\mu$m in the model, $R_{toa}$ drops by 0.055, $A_{col}$ increases by 0.048, and $A_{sfc}$ changes by only 0.007. Therefore $R_{toa}$ and $A_{col}$ are sensitive to $D_e$ ($\Delta R_{toa}/\Delta D_e = -0.07\%/\mu$m, $\Delta A_{col}/\Delta D_e = +0.06\%/\mu$m), while $A_{sfc}$ is nearly independent of $D_e$. When fluxes for each of the 12 cases are calculated using the individual $D_{e37}$ inputs (FL37 in Figure 5), individual case results vary, but the average results remain similar to what is obtained using a constant $D_e$ = 60 $\mu$m. This result suggests that the model-calculated $R_{toa}$ and $A_{col}$ with the input of individual $D_e$ values are statistically the same as those with fixed $D_e$ = 60 $\mu$m. This is consistent with the fact that, to first order, absorption in the cloud layer for the optically thick limit is linear in cloud particle diameter.

[28] Using the 2.1-$\mu$m retrievals as inputs, the model calculations (FL21 in Figure 5) agree with the observations to within <0.007 for $R_{toa}$, and 0.018 for $A_{col}$. How do we judge which particle size to use: 3.7 or 2.1? The ARM radar vertical profiles of $D_e$ suggest increasing particle size from cloud top to bottom by 33% (120$\mu$m/90$\mu$m), while Figure 6 shows that the 2.1-$\mu$m channel will respond to cloud particles lower in the cloud layer than 3.7-$\mu$m channel. The total solar absorption will see over a greater depth into the cloud than the absorption at 2.1-$\mu$m. The ratio of satellite-derived cloud particle size $D_{e21}/D_{e37}$ = 1.58 from Figure 5 is even larger than the ratio of 1.33 found using the ARM radar. Recall, however, that the ARM radar derived cloud top is attenuated at 10 km, while the satellite 11-$\mu$m emission temperature is higher at 12.3 km (Table 1). The visible optical depth at this emission level is typically about 2, similar to the level expected for the 3.7-$\mu$m particle size retrieval. This suggests that the larger satellite ratio is a simple result of the satellite sensing higher in the cloud at 3.7-$\mu$m channel, and that a radar capable of sensing particle size to the higher altitude would see a larger top/bottom particle size ratio. It should be possible in future analysis of the lidar/radar cloud top view of CALIPSO/CloudSat to gain further insight into the vertical profile of $D_e$ in the upper several kilometers of tropical ice clouds. We also note that the average $D_{e21}$ value of 104 $\mu$m is within the 30% uncertainty of the 120 $\mu$m ARM radar value in the lower half of the convective cloud layer. The above discussion clearly indicates that the $D_{e21}$ retrievals are more appropriate cloud microphysical properties to use in calculations of the DCS radiation budgets. They represent the minimum $D_e$ appropriate for broadband absorption calculations. The ratio $D_{e21}/D_{e37}$ is shown to be remarkably stable for all 12 cases in Figure 5, suggesting that the relative vertical distribution

**Table 5.** Sensitivity of Cloud-Radiation Properties on $\tau$ at the SGP Site (Averages and 95% Confidence Intervals)

| Samples (Terra and Aqua) | $\tau$ | $R_{TOA}$ | $A_{sfc}$ | $A_{COL}$ |
|---|---|---|---|---|
| 182 for $\tau > 15$ | 37 (±2.6) | 0.594 (±0.008) | 0.121 (±0.008) | 0.285 (±0.006) |
| 108 for $\tau > 30$ | 48 (±3.2) | 0.625 (±0.008) | 0.096 (±0.008) | 0.279(±0.008) |
| 67 for $\tau > 40$ | 57 (±4.1) | 0.642 (±0.009) | 0.083 (±0.009) | 0.275(±0.009) |
| 35 for $\tau > 50$ | 68 (±6.0) | 0.661 (±0.010) | 0.064 (±0.009) | 0.275 (±0.009) |
| 16 for $\tau > 60$ | 82 (±9.7) | 0.675 (±0.015) | 0.058 (±0.018) | 0.266 (±0.015) |
| 10 for $\tau > 70$ | 93 (±9.3) | 0.689 (±0.016) | 0.047 (±0.023) | 0.264 (±0.017) |
| 8 for $\tau > 80$ | 97 (±9.2) | 0.693 (±0.017) | 0.037 (±0.018) | 0.270 (±0.018) |

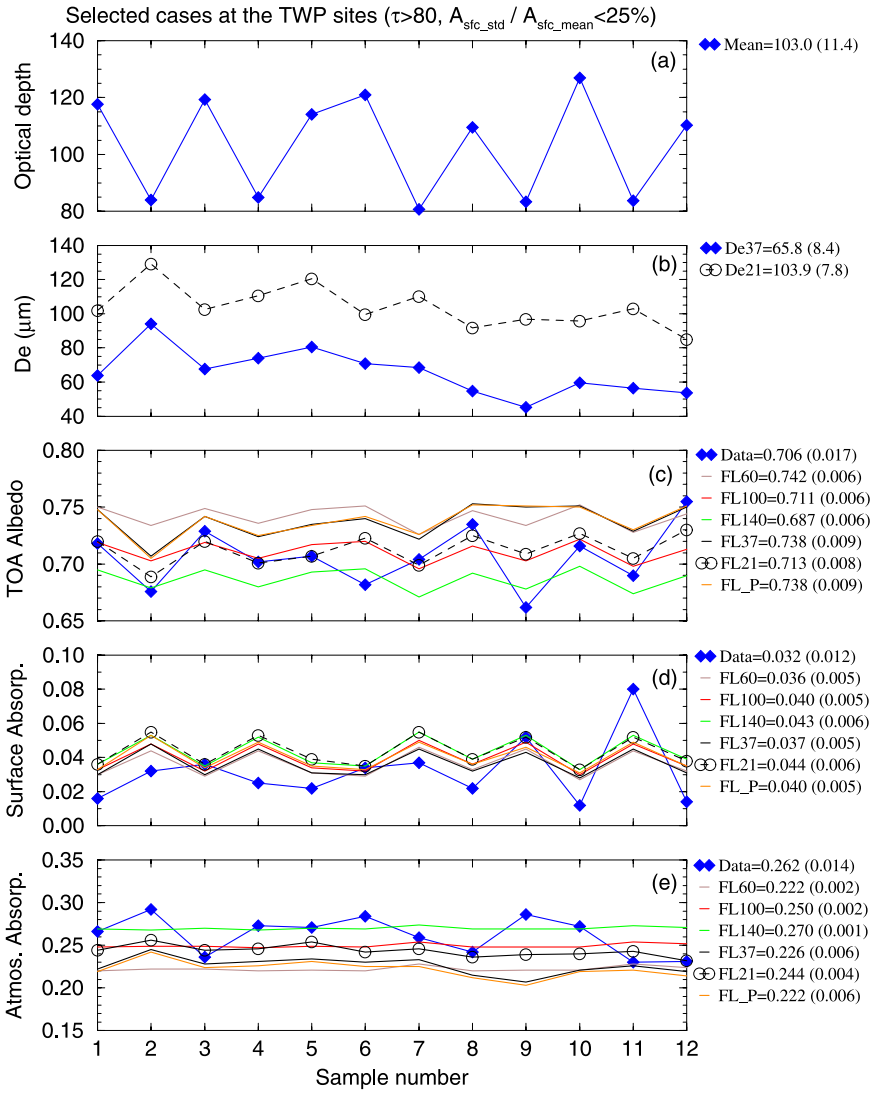


**Figure 5.** (a) and (b) represent the CERES-MODIS-retrieved $\tau$ and $D_e$ (at $\lambda = 3.7$ $\mu$m for $D_{e37}$ and $\lambda = 2.1$ $\mu$m for $D_{e21}$) mean values (95% confidence interval), and the blue diamonds in (c), (d) and (e) are observations or derived from observations. FL60, FL100, FL140 are calculated from the Fu-Liou code with the inputs of the CERES-MODIS-retrieved $H_e$ and $\tau$, as well as fixed layer-mean $D_e$ = 60/100/140 $\mu$m, $R_{sfc}$ = 0.064, $\mu_0$ = 0.9, $\tau_{\text{aerosol}}$ = 0.2, and standard tropical sounding. FL37 and FL21 are calculated with each individual $R_{sfc}$, $\mu_0$, layer-mean $D_e$ values at $\lambda = 3.7$ $\mu$m and $\lambda = 2.1$ $\mu$m, respectively, for the 12 re-selected DCS cases. The inputs of FL_P are the same as those of FL37 except for the vertical profiles of $D_e$ and $\tau$ (10 sublayers). The satellite results are averaged over a 20-km $\times$ 20-km box and the surface observations are averaged over a 0.5-h period.

of particle size in tropical deep convection may be a robust and stable feature.

[29] The above radiative model calculations all used constant vertical particle size. For vertically varying cloud layers (FL_P in Figure 5), the model-calculated $R_{toa}$, $A_{sfc}$, and $A_{col}$ values are almost the same as those computed with the input of individual layer-mean $D_{e37}$. Since $A_{sfc}$ is insensitive to $D_e$, the $R_{toa}$ and $A_{col}$ of the entire cloud layer are mostly determined by the upper layer ice cloud microphysics where the $D_e$ values are close to or slightly exceed $D_{e37}$. In the optically thick limit, the sum of 1–4 sublayers near the cloud top has a combined $\tau$ of $\sim$10–30 that accounts for about 80–90% of shortwave $A_{col}$ as shown in Figure 6; that is, there are not many solar photons left to penetrate into deeper cloud layers. Therefore the ARM-derived vertical profiles of ice cloud microphysics cannot improve the calculations of radiation budgets much in the optically thick limit, but are important to the cloud absorption under other cloudy conditions. The model also calculates $A_{col}$ spectrally, revealing that most of the solar photons are absorbed at wavelengths of 1–4 $\mu$m by the ice crystals near the cloud top ($\tau < 10$ as shown in Figure 6). Although the ARM microwave radiometer-retrieved *LWP* values are large at both the TWP and SGP sites, the liquid water is located near the bottom part of the DCS where few solar photons remain. With the second and third types of inputs (FL37 and FL_P), the differences between observed and model-calculated surface absorption, on average, are less

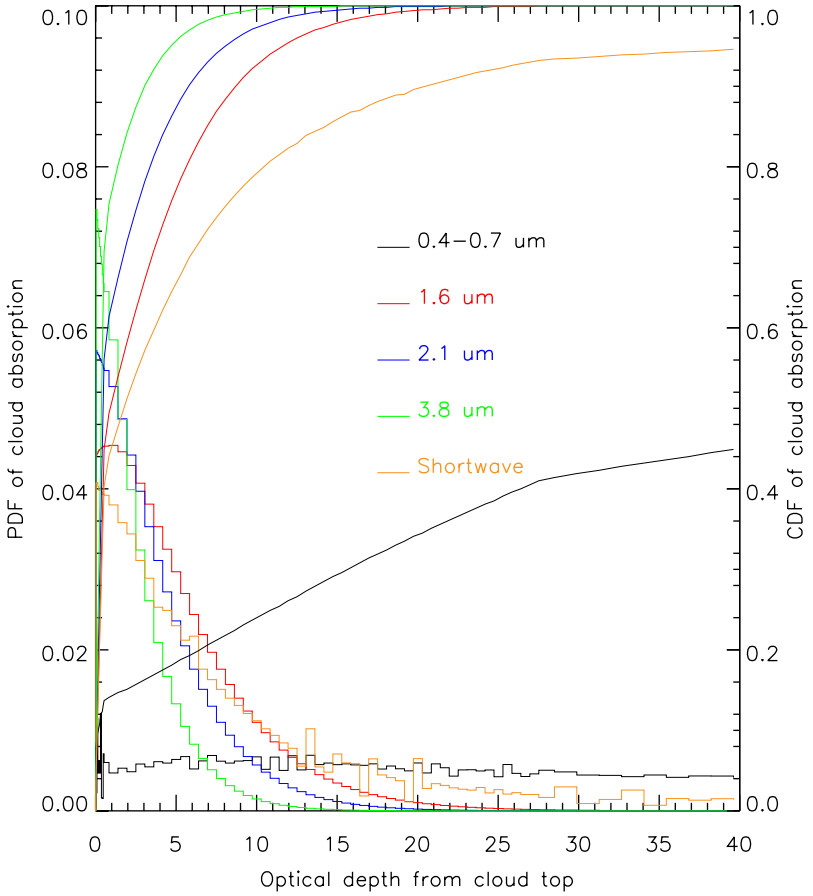


**Figure 6.** Probability Distribution Functions (PDF) and Cumulative Distribution Functions (CDF) of solar photons at visible, 1.6-$\mu$m, 2.1-$\mu$m, 3.8-$\mu$m, and broadband shortwave channels be absorbed by ice cloud particles from the cloud top ($\tau = 0$). The PDF and CDF were calculated by the DISORT radiative transfer model [*Stamnes et al.*, 1988] with the correlated-k assumption [*Kato et al.*, 1999]. The cloud top height was set up at 15 km with the vertical resolutions of 10 m from 15 km to 14 km and 100 m below 14 km. An ice crystal distribution (FIRE-II) described by *Nasiri et al.* [2002], the extinction coefficient of 5.56 $km^{-1}$, the solar zenith angle of 0 degree, and standard tropical atmosphere were used in the model.

than 0.01, but the model-calculated $R_{toa}$ and $A_{col}$ are 0.032 higher and 0.04 lower, respectively, than the observed values. However, the differences are reduced to 0.007 and 0.018, respectively, by using $D_{e21}$ as input.

[30] The uncertainty or "error" in modeling $A_{col}$ (with $D_{e21}$) is 0.018 out of 0.262. This relative difference in column absorption of 7% is even less than the 10% consistency in the *Ackerman et al.* [2003] cases. It is also useful to scale the difference in $A_{col}$ of 0.018 in terms of global average flux. In this metric, the difference of 0.018 in $A_{col}$ is equivalent to a change in global mean column atmosphere absorbed flux of 6.1 $Wm^{-2}$ [(0.262–0.244) * 341 $Wm^{-2}$], an order of magnitude smaller than the 25–30 $Wm^{-2}$ values found in the *Cess et al.* [1995, 1996] studies. The current results, however, deal only with the optically thick overcast ice cloud cases.

[31] Finally, since as discussed above even $D_{e21}$ is a lower bound on $D_e$ for the radiative calculations, it is relevant to ask how much larger a particle size would be consistent with the $R_{toa}$ observation? $D_{e21}$ would have to be increased by 12%, or from an average of 104 to 116 $\mu$m, a value very close to the ARM radar value of 120 $\mu$m in the lower half of the convective cloud. In this case, the average radiative model calculated $A_{col}$ increases from 0.244 to 0.251, with the difference from observations reduced from 0.018 to 0.011, or a relative error of only 3% of the column absorption.

## 5. Uncertainty Analysis

[32] Tables 2–5 and Figures 1–5 document the variability of the cloud and radiation observations, while section 4 quantified the uncertainties and sensitivity of the radiative model used. The final question is then: are the radiative model calculations within the uncertainty of the observations? This question requires an analysis of not just observation variability, but also estimates of systematic biases and random errors in the observations: both fluxes as well as cloud properties used as input to the radiative model. While a full end-to-end error analysis is beyond the scope of this paper, we cover the major elements of such an analysis below. We focus our efforts on the optically thick cases shown in Figure 5, as they showed the lowest variability in matching satellite and surface data.

**Table 6.** Summary of Error Sources for the $\tau > 80$ Cases in Figure 5

| | $R_{toa}$ | | $A_{sfc}$ | | $A_{col}$ | |
|---|---|---|---|---|---|---|
| Observation Error Sources | Bias | Sigma | Bias | Sigma | Bias | Sigma |
| CERES SW Albedo | 0.008 | 0.021 | - | - | 0.008 | 0.021 |
| Surface Pyranometer | - | - | 0.003 | 0.002 | 0.003 | 0.002 |
| Surface Albedo | - | - | 0.001 | 0.001 | 0.001 | 0.001 |
| Solar constant | 0.002 | 0.001 | - | - | 0.002 | 0.001 |
| Sat/Sfc Space&Time Match | 0.000 | 0.000 | 0.000 | 0.015 | 0.000 | 0.015 |
| Total observation uncertainty ($\sigma^{obs}_{total}$ for 12 case avg) | 0.008 | 0.006 | 0.003 | 0.005 | 0.009 | 0.008 |
| Observation 95% confidence (for 12 case avg) | ± 0.021 | | ± 0.012 | | ± 0.024 | |
| Modeling error sources | Bias | Sigma | Bias | Sigma | Bias | Sigma |
| MODIS cloud optical depth | 0.008 | 0.021 | 0.009 | 0.021 | 0.002 | 0.000 |
| MODIS ice particle diameter | 0.009 | 0.003 | 0.001 | 0.000 | 0.009 | 0.003 |
| Radiative model consistency | 0.005 | 0.000 | 0.000 | 0.000 | 0.005 | 0.000 |
| Total model uncertainty ($\sigma^{model}_{total}$ for 12 case avg) | 0.013 | 0.006 | 0.009 | 0.006 | 0.010 | 0.001 |
| Model 95% confidence (for 12 case avg) | 0.029 | | 0.023 | | 0.020 | |
| Model−observations (95% confidence) | 0.036 | | 0.026 | | 0.031 | |
| Model−observation mean difference | +0.007 (1%) | | +0.012 (30%) | | −0.018 (7%) | |

[33] A summary of the error budget terms and their values can be found in Table 6. A consideration of the error sources listed in the table and discussed in the following sections supports the assumption that the error sources are independent. While both bias and random uncertainties are considered separately, each are independent statistical variables. Bias error is usually considered to be some fixed value, such as a percent error in calibration of the CERES SW radiance. This value is in fact unknown, with only some confidence level associated with it. For most calibration biases, if the confidence level is not specified, it is 1-sigma or roughly 60% confidence that the true calibration bias is within the specified range. Except where specified as 95% confidence bounds, all values in Table 6 are given as $1\sigma$ uncertainty whether bias or random components. Table 6 is divided into two sections, the upper half for observation uncertainty, and the lower half for modeling uncertainty. Within each section, the variance ($\sigma^2$) of error sources within a column are summed to obtain a total variance ($\sigma^2_{total}$) for an individual case. The variance of the average of all 12 cases in Figure 5 is given by $(\sigma^2_{total})/11$, where the 12 cases are independent samples. For bias errors, there is no reduction with number of cases, but the variance of uncertainty in multiple bias error sources applies as for random errors.

[34] To estimate 95% confidence bounds on the average values in Figure 5, a Student's-T value of 2.2 is used for the random components (11 degrees of freedom). For bias errors the $1\sigma$ uncertainty is doubled to $2\sigma$. Note that since bias and random error sources are independent physically, we treat them as independent variables whose variance can be summed. In this way a final 95% confidence estimate is made that includes both the bias and random components. If the reader is interested in a less stringent confidence bound of ~60%, reduce the 95% confidence values in Table 6 by a factor of 2.

[35] Since the difference between an observation and the model is simply the difference of two random variables, the total variance of observations and modeling are added to estimate the variance in their difference. Thus the final two rows of Table 6 give the average value from Figure 5 for observations and model calculations (FL21) as well as the 95% confidence in their difference.

[36] Sections 5.1 through 5.6 summarize the error estimates used in Table 6. Section 5.7 discusses final results of Table 6, as well as the implications of the error analysis for future studies to further narrow the uncertainty in radiative closure for the optically thick limit.

### 5.1. Uncertainty in Observations of $R_{toa}$ and $A_{sys}$

[37] For $R_{toa}$, the uncertainty in TOA solar insolation is negligible. The most common value currently used for annual average solar constant is 1365 $Wm^{-2}$, with recent SORCE active cavity satellite observations suggesting a value as low as 1361 $Wm^{-2}$, but even this difference is only 0.3% relative bias uncertainty. The 0.3% is also large enough to include daily and 11-year cycle variability in solar constant, so we will use this as the upper bound for TOA solar insolation uncertainty.

[38] Uncertainty in broadband reflected $SW_{toa}$ flux is larger. Absolute calibration uncertainty of the CERES broadband SW radiance is estimated as 1%, $1\sigma$ [*Priestley et al.*, 2002; *Matthews et al.*, 2005]. Random instrument noise is much less than 1%. Uncertainty in the radiance to flux conversion (i.e., ADMs) for optically thick ice clouds is estimated to be 3% of the reflected TOA SW flux ($1\sigma$), with bias errors less than 0.5% [*Hu et al.*, 2004; *Loeb et al.*, 2003b].

[39] We conclude that for $R_{toa}$ in these cases, bias error is dominated by CERES SW radiance absolute accuracy of 1% in SW radiance, while random errors are dominated by the 3% ADM random error. Total bias error is estimated as $(0.3^2 + 1.0^2 + 0.5^2)^{1/2} = 1.1\%$ relative in $R_{toa}$. Random error is 3% relative. Given the average value of $R_{toa} \sim 0.7$ for the cases in Figure 5, we obtain a bias error in $R_{toa}$ of 0.008, and a random $1\sigma$ uncertainty of 0.021 for each individual case. Since $A_{sys}$ is simply $1 - R_{toa}$, the uncertainties in $A_{sys}$ are the same as those for $R_{toa}$.

### 5.2. Uncertainty in Observations of $A_{sfc}$

[40] For $A_{sfc}$ there are three observed components. For simplicity in the error analysis, we convert the definition of $A_{sfc}$ in (2) to an equivalent form: $A_{sfc} = SW^{\downarrow}_{sfc}(1 - SW^{\uparrow}_{sfc}/$

$SW^{\downarrow}_{sfc})/SW^{\downarrow}_{toa} = SW^{\downarrow}_{sfc}(1 - R_{sfc})/SW^{\downarrow}_{toa}$. In this way we can more simply combine the relative % error sources in each term. Uncertainties in TOA solar insolation are the same as those derived above: 0.3% relative bias. Uncertainties in the downward SW flux observation for these optically thick cases will be dominated by the diffuse pyranometers, since the direct beam insolation at the surface is essentially zero. For these instruments, absolute accuracy (bias in instrument gain) is estimated as 1.5% [*Dutton et al.*, 2006], which would be less than 2 $Wm^{-2}$ for the low insolation values shown in Table 2, and even lower for the optically thicker cases in Figure 5. Instead, the dominant bias error in the surface insolation is likely from thermal offsets. For clear-sky cases these effects can be as large as 10 $Wm^{-2}$, but are thought to be much less than this for diffuse cloudy sky conditions [*Dutton et al.*, 2004]. We assume a value of 5 $Wm^{-2}$ is reasonable for the low insolation cases used in this study. In relative percentage, this represents about 5% of the SW insolation for the cases in Figure 5.

[41] Finally, the surface albedo $R_{sfc}$ uncertainty will be dominated by the variable percentage of land and ocean in the satellite data over the TWP site cases, and by the uncertain average of surface albedo over the island region. We conservatively estimate this uncertainty as 20% of the value of $R_{sfc}$. Since the term in (2) is (1-$R_{sfc}$), and since the average value of $R_{sfc}$ is only 0.08 (Table 2), the relative percentage error in the term $(1 - R_{sfc})$ is estimated as 100 $(0.2\ R_{sfc})/(1 - R_{sfc}) = 2\%$. In effect, the low surface albedo of 8% reduces the relative impact of surface albedo error by a factor of 10. We finally conclude that the total percentage error in $A_{sfc}$ is given by $(5^2 + 2^2 + 0.3^2)^{1/2} = 5.4\%$ relative uncertainty in $A_{sfc}$. The dominant error source is the thermal offset uncertainty in the surface radiometer. Note, however, that since the average value of $A_{sfc}$ for the optically thick cases in Figure 5 is only 0.032, that this represents a very small uncertainty in $A_{sfc}$ of (0.032)(0.054) = 0.002. This is a very tight constraint and its low value is primarily a benefit of using the optically thick limit cases in this study.

### 5.3. Space and Time Mismatches of Surface and TOA Radiative Fluxes

[42] Estimates of $A_{col}$ from observations in this study require space and time matched estimates of $R_{toa}$ from satellite observations and $R_{sfc}$ from the surface observations. In general, the large difference in satellite and surface radiometer fields of view will mean that each radiometer is responding to significantly different cloud fields, especially for cloud optical depth and cloud fraction. Even in the overcast ice cloud cases used here, which eliminate cloud fraction inconsistencies, some level of optical depth inconsistencies will remain. If these dominate the variability, then we would expect the variability of $R_{toa}$ and $A_{sfc}$ to be similar, as they are in Figures 1 and 3 which only restrict cases to overcast $\tau > 15$. However, in the optically thick limit, $R_{sfc}$ approaches zero, and its variability will reduce. This is seen in Figure 5, where the mean value of $A_{sfc}$ drops to 0.032, and the variability as evidenced by 95% confidence in $R_{toa}$ is 50% larger than the confidence in $A_{sfc}$. This argues that we should not expect the variability in $A_{sfc}$ for the optically thickest cases to be entirely captured by variations in cloud optical depth or cloud particle size seen by the satellite during its overpass of the surface site. We estimate the magnitude of this effect, by assuming that the difference in the 95% confidence bound between the observed $A_{sfc}$ value (0.012), and that for the FL21 radiative calculations (0.006) is explained primarily by space/time mismatch of the satellite and surface cloud fields. Under this assumption, we find that the space/time mismatch noise for $A_{sfc}$ has a $1\sigma$ value of 0.015.

### 5.4. Uncertainty in Observations of $A_{col}$

[43] Finally, the uncertainty in the observed value of $A_{col}$ from equation (2) is the sum of uncertainties in $R_{toa}$ and $A_{sfc}$. Combining all of the independent observation uncertainty sources from Table 6, bias error for $A_{col}$ is then $(0.008^2 + 0.003^2 + 0.001^2 + 0.002^2)^{1/2} = 0.009$. Random error is $(0.021^2 + 0.002^2 + 0.001^2 + 0.001^2 + 0.015^2)^{1/2} = 0.026$ These are 1-sigma confidence levels for each individual satellite/surface pair observation of $A_{col}$.

[44] The uncertainties in $A_{col}$ are dominated by three components; CERES absolute calibration, radiance to flux conversion noise, and space/time matching noise. The last two of these could be eliminated by gathering an order of magnitude more cases at additional surface sites over longer time periods. This would reduce the total uncertainty by a factor of 2. Note that in the optically thick limit, the surface radiometers do not have to be very accurate, as the signal level is very small. In this case the much larger number of less accurate GEBA or other surface sites might be used for satellite matches. The absolute calibration uncertainty in $R_{toa}$ will remain until some mission similar to the recent NRC Decadal Study CLARREO mission can achieve higher levels of solar and infrared spectral absolute calibration and extend them to broadband radiometers like CERES.

### 5.5. Uncertainties in Radiative Model Input: Visible Optical Depth

[45] We now turn to uncertainties in the radiative model cloud property input. For the optically thick overcast cases in Figure 5, there are only 2 cloud properties that will dominate the radiative calculations: $\tau$ and $D_e$. In the limit of infinite optical depth, there is no sensitivity of the radiative model calculations to cloud optical depth. However, have the clouds in Figure 5 reached this limit? At the optically thick limit for extensive ice cloud anvils, the uncertainty in visible optical depth is most likely controlled by the absolute calibration uncertainty of the MODIS radiometer visible channel. This uncertainty is estimated at 1.7% [*Xiong et al.*, 2005] for the 0.65 $\mu$m visible channel used here. The 1.7% calibration uncertainty is considered to be a 1-sigma confidence bound (Xiong, personal communication), similar to the CERES 1% absolute SW radiance calibration uncertainty. The 1% difference between the Aqua and Terra MODIS 0.65-$\mu$m calibrations [*Minnis et al.*, 2008] reflects the absolute calibration uncertainty. For the 103 optical depth average in Figure 5, this $1\sigma$ confidence bound on MODIS visible channel calibration gives an optical depth uncertainty range of ~80 to 130. This estimate was made using the Fu-Liou radiative transfer model for the 0.6 to 0.7 $\mu$m spectral band similar to the MODIS visible channel. Changing visible optical depth from the 100 value in Figure 5 to 130 increases broadband albedo calculations by ~+0.007, while decreasing $\tau$ to 80 drops

$R_{toa}$ by −0.008. We conclude that even a 1.7% uncertainty in MODIS calibration is reduced to approximately an 0.8% uncertainty range for $R_{toa}$ for the clouds in Figure 5. Using a similar modeling sensitivity study we set the $1\sigma$ MODIS optical depth bias error for $R_{toa}$ as 0.008, $A_{sfc}$ as 0.009, and $A_{col}$ as 0.002. Note that these uncertainties would be much larger for typical optical depth clouds ($\tau \sim 3$ to 10), which have a roughly linear relationship of visible to broadband albedo, or for broken cloud cases with optical depth errors due to 3-dimensional cloud structure.

[46] Random errors for the MODIS cloud optical depth will be dominated by uncertainties in ice particle habit and 3-D cloud structure. Both effects will vary with satellite viewing geometry. In the optically thick limit for large ice cloud anvils near the tropopause, both of these effects are minimized. While these effects are implicitly included in the average anisotropy of observed CERES ADMs for thick ice clouds, their effect is not explicitly included in the radiative model calculations. For the ice particle habit effect, *Mishchenko et al.* [1996] examined the dependence of visible channel bidirectional reflectance on the difference between hexagonal and fractal ice crystal shapes. For large optical depths (300) at the solar zenith and viewing angles used in this study, they found less than 5% relative change in reflectance. No equivalent study of radiance variability has been done for horizontal and vertical variations in large scale deep convective anvils. Since both of these effects will also drive random variability in the CERES ADMs, with a similar relative magnitude, we use the ADM variability observed by CERES for the deep convective clouds as the best overall estimate of noise in the MODIS optical depth retrievals. We also note that *Hu et al.* [2004] found that the CERES ADMs for these same cloud types agreed very well with DISORT radiative model calculations using hexagonal crystal particle shapes and horizontally uniform clouds. This again suggests small 3-D and ice crystal habit uncertainties for these cases. Future combined analysis of the A-train CALIPSO lidar, CloudSat radar, CERES, and POLDER multiangle visible data could provide more rigorous tests of this assumption for the optically thick limit ice clouds in the future.

### 5.6. Uncertainties in Radiative Model Input: Ice Particle Effective Diameter

[47] The second key cloud property input to the radiative model is the cloud particle size, specified here as an effective diameter $D_e$. As discussed in section 4, from the radiative model calculations shown in Figure 5, the impact of changing cloud particle size for the optically thick limit from $D_e$ of 60 to 100 to 140 $\mu$m is to change $R_{toa}$ from 0.742 to 0.711 to 0.687, for a total change of −0.055. The total change in $A_{sfc}$ for the same change in particle size is only +0.007, while $A_{col}$ is +0.048. As indicated earlier, the decrease in $R_{toa}$ is directly related to the increase in $A_{col}$. Note that in the limit of optically thin cloud the opposite happens: changes in $R_{toa}$ are instead directly related to changes in $A_{sfc}$, and not in $A_{col}$. In the optically thin case, water vapor dominates $A_{col}$ instead of cloud particle absorption as in the current study. The absolute uncertainty of ice particle size is complicated by issues of particle shape, bimodal versus monomodal size distributions, and by ice particle density. A recent comparison of cloud radar derived ice particle size retrievals with in situ aircraft data concluded that a consistency of 40% was typical [*Mace et al.*, 2002]. Comparisons of cloud radar-derived ice particle size with satellite retrievals showed biases of 10% and standard deviation of 30% [*Mace et al.*, 2005]. This comparison included the CERES-MODIS $D_e$ retrievals used in this study, but was over the ARM SGP site and included only thin cirrus with optical depth less than 4. The particle sizes observed, however, were similar to the 60 $\mu$m $D_{e37}$ values found for TWP and SGP thick ice clouds in this study. We are left to conclude, however, that a first principle tie of satellite retrieved $D_e$, through the ARM radar to aircraft can only currently be claimed to be roughly 40%, limited by the validation data accuracy of aircraft in situ data to ARM radar data, and the need for tests in a wider range of ice cloud optical thickness. When added to the average variation in particle size from cloud top to bottom of 30% discussed in section 4, the total uncertainty is $(30^2 + 40^2)^{1/2} = 50\%$ in $D_e$. Using the radiative model sensitivity discussion above, this would lead to a large uncertainty in $R_{toa}$ and $A_{col}$ of ±0.03 and would dominate all other error sources.

[48] There is an alternative way to constrain uncertainty in $D_e$. The radiative transfer theory that underlies the broadband albedo calculations for cloud absorption is the same as the theory that underlies the satellite cloud particle size retrieval. For particles much larger than the wavelength of radiation considered, anomalous diffraction theory predicts that particle absorption cross-section at a given wavelength is essentially linear in the product of particle size and the imaginary index of refraction for the particle material, which in this case is ice. As a result, cloud absorption optical depth and co-albedo (1 minus single scatter albedo) are also monotonic functions of $D_e$ and $(1 - \omega)$ as well. In the optically thick limit, near-infrared wavelength reflectance will be monotonically related to cloud particle size, and this is the basis of the physics of cloud particle size retrieval using near-infrared wavelengths [e.g., *King et al.*, 1992].

[49] The same absorption physics determines broadband absorption of solar radiation, but at all solar wavelengths as opposed to a narrow spectral band used for satellite particle size retrieval. In the optically thick limit the reflectance at these wavelengths is dominated by particle absorption, with little dependence on particle habit or scattering phase function. This is easy to understand by considering the common scaling of scattering optical depth using asymmetry parameter to derive an effective scattering optical depth. We showed earlier that in the optically thick limit, $R_{toa}$ and $A_{col}$ are independent of visible scattering optical depth and therefore asymmetry parameter has very little effect on absorption. We conclude from this discussion, that the CERES-MODIS retrieved particle size $D_e$ is precisely the estimate needed for the radiative model calculation of broadband solar absorption providing that (a) uncertainties in imaginary refractive index as a function of wavelength are small, (b) the satellite retrieval wavelength is similar to the near-infrared wavelengths that dominate cloud particle solar broadband absorption, (c) the MODIS spectral channel calibration is accurate, and (d) consistent definitions of particle size and imaginary index of refraction are used in the cloud retrieval radiative transfer and in the broadband

flux radiative transfer codes. Uncertainties for these sources are estimated below.

[50] (a) Imaginary index of ice uncertainties in the near-infrared are estimated to be ~5 to 10% [*Kuo et al.*, 1993]. If all wavelengths are systematically high by 10%, then the satellite-retrieved particle size will be low by 10%, resulting in essentially the same broadband solar absorption. However, if the wavelength used for satellite cloud retrieval has an error different than the remainder of the near-infrared solar spectrum, then we would expect errors in the broadband solar absorption modeling, since the particle size and absorption in the satellite narrowband channel would not be representative of the remainder of the near-infrared solar spectrum. For the current analysis, we assume a worst case scenario that the error in the satellite retrieval channel will differ by 10% from the imaginary index error at other wavelengths. This will cause an error of 10% in the particle size used for the radiative model calculations. Using the sensitivity to particle size in Figure 5 cases FL60, FL100, and FL140 with 60/100/140 $\mu$m $D_e$ values, a 10% particle size error will cause an error in $A_{col}$ and $R_{toa}$ of ±0.006.

[51] (b) The CERES-MODIS retrieved $D_e$ values shown in the tables and figures use a 3.7-$\mu$m wavelength which is in the near infrared, but not in the primary solar absorption region from 1 to 3 $\mu$m. In this case, the particles absorbing at 3.7 $\mu$m will be near the top of the cloud, while the bulk of the near-infrared absorption, such as at 1.6 and 2.1 $\mu$m, will be deeper in the cloud as shown in Figure 6. We conclude that the 2.1-$\mu$m satellite-derived particle size is more appropriate than 3.7-$\mu$m $D_e$ for radiative model calculations of solar absorption in the current paper. For the cases in Figure 5, $D_e$ increases from 65.8 (at $\lambda = 3.7$ $\mu$m) to 103.9 $\mu$m (at $\lambda = 2.1$ $\mu$m). These values are close to the case FL100 with $D_e$ = 100 $\mu$m. Because of this uncertainty in the optimal satellite narrowband wavelength that should be used for an equivalent broadband absorption estimate, we use an uncertainty of 15% in $D_e$. This is the fractional difference in the vertical particle size changes from cloud bottom to cloud top estimated as 1.35 from the ARM radar TWP data, and estimated as 1.54 for the MODIS retrieved $D_{e21}/D_{e37}$. Scaling from the particle size sensitivity as in error a) above, this gives an uncertainty in $R_{toa}$ and $A_{col}$ of ±0.009.

[52] (c) The MODIS spectral channel calibrations for the near-infrared channels such as 2.1 $\mu$m are estimated to have an absolute accuracy of 3% in reflectance, which is the quantity that will control the retrieved particle size. Given the roughly linear relationship at this wavelength between reflectance and particle size, this suggests a 3% uncertainty in particle size purely from calibration. Using the particle size sensitivity of broadband solar absorption as in error sources (a) and (b), this 3% particle size uncertainty gives an uncertainty in the calculated broadband $R_{toa}$ and $A_{col}$ of ±0.002.

[53] (d) The satellite cloud particle retrieval radiative transfer codes and the modified Fu-Liou radiative code employed in this study use consistent definitions of $D_e$ and imaginary indices of refraction for ice. A conversion between the $D_e$ definition used in the satellite retrieval to the $D_{ge}$ definition used in the original Fu-Liou code is applied to achieve consistent particle size. As the particle sizes considered in this study, the relationship is roughly linear with $D_e$ being larger by about 20%. The modified Fu-Liou code converts the $D_e$ value into $D_{ge}$ for the radiative modeling predictions. As a result, there are no inconsistencies that require correction in this study between the satellite $D_e$ values and their use in the modified Fu-Liou radiative transfer model.

[54] We conclude that model input errors for $D_e$ as discussed in items (a) through (d) above result in a total uncertainty for radiative calculations of $R_{toa}$ and $A_{col}$ of $(0.006^2 + 0.009^2 + 0.002^2)^{1/2} = \pm 0.011$. This is a factor of 3 tighter constraint than the current ability to constrain uncertainties using satellite $D_e$ retrievals validated against ARM radar which is in turn validated against aircraft in situ data. Finally, we combine this particle size uncertainty with the cloud visible optical depth uncertainty from section 5.5 to obtain a total radiative model input uncertainty for $R_{toa}$ and $A_{col}$ of $(0.011^2 + 0.012^2)^{1/2} = 0.016$.

### 5.7. Uncertainty Analysis Conclusions

[55] The differences between observations and model calculations for $R_{toa}$, $A_{sfc}$, and $A_{col}$ are all within 95% confidence bounds. The differences for $R_{toa}$ and $A_{sfc}$ are also within 60% confidence bounds. The 95% confidence bounds do not, however, rule out column absorption issues of magnitude smaller than 0.03, which represents a time averaged global atmospheric absorption of 10 $Wm^{-2}$. While this makes the result one of the most stringent tests to date, further improvements are desired, down to at least the level of 0.01 or about 3 $Wm^{-2}$.

[56] The uncertainty analysis in Table 6 has the ability to quantify and prioritize the improvements needed to reduce uncertainty in $A_{col}$ from 0.03 to 0.01. Considering $\sigma_{\text{total}}$ for the observations in Table 6, both random and bias errors must be reduced.

[57] The two major random errors are ADM errors in $R_{toa}$ and time/space matching errors in $A_{sfc}$. A factor of 10 more independent cases will be required to reduce these by a factor of 3. Within a few years, a factor of 2 increase in the number of samples will be available from a longer record of CERES overflights of the ARM TWP sites. An additional 10 BSRN and GEBA tropical surface sites could provide the remaining sampling increase. Note that while the measurement accuracy of GEBA surface radiation sites is much lower than at the ARM or BSRN sites, the surface fluxes in the optically thick limit are very low and high accuracy is not required.

[58] For bias errors, the uncertainty is dominated by CERES and MODIS calibration and by uncertainty in the vertical distribution of cloud particle size in the upper parts of the convective cloud anvil. For calibration, absolute accuracy of 0.3% ($1\sigma$) for the CERES broadband SW radiance, and 0.6% ($1\sigma$) for the MODIS visible channel would be required. Future planned observations from the Climate Absolute Radiance and Refractivity Observatory (CLARREO) mission proposed in the recent NRC Decadal Survey for Earth science include a goal to allow calibration of future MODIS and CERES equivalent instruments to reach this accuracy level or better. Since CLARREO will only view a 100-km nadir field of view, however, the number of space/time matched overflights of surface sites will drop by an order of magnitude relative to full-swath instruments such as MODIS and CERES. For low Earth orbiting satellites, ground tracks are separated in the tropics

by over 2000 km, so that CLARREO would tend to overfly one of the ARM sites roughly once every 20 days. In this case, the CLARREO solar spectra themselves will not be sufficient, but its calibration of other broadband and narrowband sensors would be sufficient.

[59] Reducing the bias error from uncertainty in the vertical distribution of particle size will require either more powerful surface radars that are not attenuated in these optically thick limit convective clouds, or use of the top-down view of the CALIPSO lidar and CloudSat cloud radar data. From Figure 6, most of the broadband solar absorption occurs within optical depth 3 of the cloud top, and more than 80% within optical depth 10. Another way to constrain the vertical distribution of particle size would be to use MODIS-like particle size retrievals over a full spectrum of solar wavelengths. Such an approach would require absolute accuracy similar to that in the broadband SW radiance of 0.3%, and would again require calibration by the CLARREO or a similar benchmark calibration mission.

[60] We conclude that in the short term, significant progress can be made by extending the number of samples similar to those in Figure 5 from 12 to 100. In the longer term, improved absolute accuracy of calibration of the satellite sensors, and improved observations of the vertical distribution of ice particle size in the upper part of the convective anvil will be required.

## 6. Conclusions

[61] Matched surface and satellite data have been used to examine the absorption of solar radiation in the atmospheric column for the optically thick limit of high altitude ice clouds. A total of 229 cases are examined over the ARM Tropical Western Pacific island sites, along with a total of 182 cases over the ARM Southern Great Planes central facility site. All cases are for overcast high altitude ice clouds with visible optical depths greater than 15. Conclusions are summarized below:

[62] (1) The DCSs at both the TWP and SGP sites have very similar cloud base heights ($\sim$1 km), but the cloud top heights at the TWP sites ($\sim$10 km) are typically about 1 km higher than those over the SGP. The averaged $D_e$ values at the TWP and SGP sites are comparable (66 $\mu$m versus 52 $\mu$m), but the averaged *LWP* at the TWP is about 5 times as large as that at the SGP site. As demonstrated in Tables 2 and 3, the seasonal variations of cloud-radiation properties at the TWP site are less than 8% relative to their annual means, while the variations are up to 61% at the SGP site. There are no strong morning (1030 LT for *Terra*) to afternoon (1330 LT for *Aqua*) DCS differences in the radiation budgets at both TWP and SGP sites.

[63] (2) The atmospheric column absorption in the Tropics is 0.01 more than that in the middle latitudes when all cases are considered, but the difference disappears for clouds with optical depths greater than 50, and when the observed column atmosphere solar absorption reaches a value of about 0.27.

[64] (3) As optical depth $\tau$ increases from 15 toward 100, the variability between cases decreases rapidly, as does the number of samples. Somewhat surprisingly, the 95% confidence in the mean value for $R_{toa}$, $A_{sfc}$, and $A_{col}$ for 12 TWP cases with optical depths greater than 80 is about the same as that for 120 TWP cases with $\tau > 30$. This suggests that the optically thick limit is a particularly useful tool for studying cloud systems with minimum variations in radiative properties. Variability at SGP for large $\tau$ was much higher than at the TWP sites, possibly as a result of more spatially extensive convective systems at TWP.

[65] (4) With the 12 optically thick cases at the TWP sites, the observations and radiative transfer calculations agree to within 0.007 (out of an average value of 0.71) for $R_{toa}$, 0.012 (out of 0.032) for $A_{sfc}$, and 0.018 (out of 0.262) for $A_{col}$. The radiative calculations use the CERES-MODIS derived visible wavelength optical depth and near infrared (2.1$\mu$m) derived effective ice particle diameter $D_{e21}$.

[66] (5) An uncertainty analysis of the observations and radiative model inputs shows that the agreement for $R_{toa}$, $A_{sfc}$, and $A_{col}$ are within the respective 95% confidence bounds of $\pm$0.036, 0.026, and 0.031. The differences are also within 70% confidence bounds of $\pm$0.018, 0.013, and 0.016 for $R_{toa}$ and $A_{sfc}$, but not for $A_{col}$. The dominant sources of bias uncertainty are the MODIS and CERES absolute calibrations along with uncertainty in the vertical distribution of $D_e$ near cloud top. The dominant sources of random error are the anisotropic correction of CERES radiance to flux, and variations from space-time matching of a surface radiometer "point" to a satellite viewing region.

[67] (6) All five of these error sources are roughly similar in magnitude, so that they all must be reduced before a narrower constraint can be made on column absorption in this optically thick limit. Fortunately improvements in all 5 are feasible. Additional BSRN and GEBA surface sites along with a greater record length of CERES/MODIS overflights can reduce sampling errors by a factor of 3. Similar or larger improvements of a factor of 3 to 10 can be made in the absolute calibration of radiometers like CERES and MODIS using observations similar to those proposed in the recent NRC Decadal Survey for the CLARREO satellite mission. The final improvement needed is a better understanding of the vertical ice particle size in the upper part of the ice cloud anvil (optical depths 0 to 10 into the cloud layer). This could be achieved by either much higher powered surface radars or by active systems such as CALIPSO and CloudSat probing from top down. Overall, the error analysis suggests that in the future it should be possible to further tighten the 95% confidence bounds between observations and theory from 0.03 to 0.01 in $A_{col}$. This would provide the tightest constraint yet envisioned for atmospheric absorption of solar radiation.

[68] This study provides a new constraint on atmospheric column absorption in the optically thick limit. It shows no evidence of unexpectedly large solar absorption, but cannot yet rule out differences up to 0.03 in absorption with 95% confidence. The study also shows clearly where future improvements could narrow this confidence to the level of 0.01 in absorption, or about 3 $Wm^{-2}$ for global average annual solar absorbed energy. The approach should be considered a very independent complement to clear-sky radiative closure studies such as those of *Ackerman et al.* [2003].

[69] **Acknowledgments.** Surface Data were obtained from the Atmospheric Radiation Measurement (ARM) Program sponsored by the U.S. Department of Energy (DOE) Office of Energy Research, Office of

Health and Environmental Research, Environmental Sciences Division. The CERES SSF products were provided by NASA Langely DAAC. Special thanks to Thomas P. Ackerman at University of Washington for providing insightful suggestions and comments, as well as continuous encouragement during this study, to Charles N. Long at DOE PNNL for providing the Best Estimate Flux Value Added Product, to Robert Cess at State University of New York, Bing Lin and Norman Loeb at NASA LaRC, Sunny Sun-Mack and Yan Chen at SSAI, and two anonymous reviewers for providing useful comments and suggestions. This research was supported by NASA CERES project under grant NNL04AA11G at the University of North Dakota.

## References

Ackerman, T. P., and G. M. Stokes (2003), The atmospheric radiation measurement program, *Phys. Today*, *56*, 38–44.

Ackerman, T. P., D. M. Flynn, and R. Marchand (2003), Quantifying the magnitude of anomalous solar absorption, *J. Geophys. Res.*, *108*(D9), 4273, doi:10.1029/2002JD002674.

Barkstrom, B. R. (1984), The Earth radiation budget experiment, *Bull. Am. Meteorol. Soc.*, *65*, 1170–1185.

Bloom, S., et al. (2005), Documentation and validation of the Goddard Earth Observing System (GEOS) data assimilation system - Version 4, in *Technical Report Series on Global Modeling and Data Assimilation 104606*, 26 pp.

Cess, R. D., et al. (1995), Absorption of solar radiation by clouds: Observations versus models, *Science*, *267*, 496–499.

Cess, R. D., M. H. Zhang, Y. Zhou, X. Jing, and V. Dvortsov (1996), Absorption of solar radiation by clouds: Interpretations of satellite, surface, and aircraft measurements, *J. Geophys. Res.*, *101*(D18), 23,299–23,309.

Chambers, L. H., B. Lin, and D. F. Young (2002), Examination of new CERES data for evidence of tropical Iris feedback, *J. Clim.*, *15*, 3719–3726.

Clothiaux, E. E., T. P. Ackerman, G. G. Mace, K. P. Moran, R. T. Marchand, M. A. Miller, and B. E. Martner (2000), Objective determination of cloud heights and radar reflectivities using a combination of active remote sensors at the Atmospheric Radiation Measurement Program Cloud and Radiation Test Bed (ARM CART) sites, *J. Appl. Meteorol.*, *39*, 645–665.

Dutton, E. G., A. Farhadi, R. S. Stone, C. N. Long, and D. W. Nelson (2004), Long-term variations in the occurrence and effective solar transmission of clouds as determined from surface-based total irradiance observations, *J. Geophys. Res.*, *109*, D03204, doi:10.1029/2003JD003568.

Dutton, E. G., D. W. Nelson, R. S. Stone, D. Longenecker, G. Carbaugh, J. M. Harris, and J. Wendell (2006), Decadal variations in surface solar irradiance as observed in a globally remote network, *J. Geophys. Res.*, *111*, D19101, doi:10.1029/2005JD006901.

Hu, Y., B. A. Wielicki, P. Yang, P. W. Stackhouse Jr., B. Lin, and D. F. Young (2004), Application of deep convective cloud albedo observation to satellite-based study of the terrestrial atmosphere: Monitoring the stability of spaceborne measurements and assessing absorption anomaly, *IEEE Trans. Geosci. Remote Sens.*, *42*, 2594–2599.

Jin, Z., T. P. Charlock, W. L. Smith, and K. Rutledge (2004), A parameterization of ocean surface albedo, *Geophys. Res. Lett.*, *31*, L22301, doi:10.1029/2004GL021180.

Jin, Z., T. P. Charlock, K. Rutledge, and K. Stamnes (2006), An analytical solution of radiative transfer in the coupled atmosphere-ocean system with rough surface, *Appl. Opt.*, *45*, 7443–7455.

Kato, S., T. P. Ackerman, J. H. Mather, and E. E. Clothiaux (1999), The k-distribution method and correlated-k approximation for a Shortwave Radiative Transfer Model, *J. Quant. Spectrosc. Radiat. Transfer*, *62*, 109–121.

Kato, S., F. G. Rose, and T. P. Charlock (2005), Computation of domain-averaged irradiance using satellite-derived cloud properties, *J. Atmos. Oceanic Technol.*, *22*, 146–164.

King, M. D., W. P. Menzel, and D. Tanre (1992), Remote sensing of cloud, aerosol, and water vapor properties from the Moderate Resolution Imaging Spectrometer (MODIS), *IEEE Trans. Geosci. Remote Sens.*, *30*, 2–27.

Kuo, L., D. Labrie, and P. Chylek (1993), Refractive indices of water and ice in the 0.65 to 0.25 um spectral range, *Appl. Opt.*, *32*, 3531–3540.

Li, Z., A. P. Trishchenko, H. W. Barker, G. L. Stephens, and P. Partain (1999), Analyses of Atmospheric Radiation Measurement (ARM) program's Enhanced Shortwave Experiment (ARESE) multiple data sets for studying cloud absorption, *J. Geophys. Res.*, *104*(D16), 19,127–19,134.

Liljegren, J. C., E. E. Clothiaux, G. G. Mace, S. Kato, and X. Dong (2001), A new retrieval for cloud liquid water path using a ground-based microwave radiometer and measurements of cloud temperature, *J. Geophys. Res.*, *106*(D13), 14,485–14,500.

Lin, B., B. A. Wielicki, P. Minnis, L. Chambers, K.-M. Xu, Y. Hu, and A. Fan (2006), The effect of environmental conditions on tropical deep convective systems observed from the TRMM satellite, *J. Clim.*, *19*, 5745–5761.

Loeb, N., et al. (2003a), Angular distribution models for top-of-atmosphere radiative flux estimation from CERES instrument on TRMM satellite, I: Methodology, *J. Appl. Meteorol.*, *42*, 240–265.

Loeb, N. G., K. Loukachine, N. Manalo-Smith, B. A. Wielicki, and D. F. Young (2003b), Angular distribution models for top-of-atmosphere radiative flux estimation from the clouds and the Earth's Radiant Energy System instrument on the Tropical Rainfall Measuring Mission satellite. Part II: Validation, *J. Appl. Meteorol.*, *12*, 1748–1769.

Mace, G. G., A. J. Heymsfield, and M. R. Poellot (2002), On retrieving the microphysical properties of cirrus clouds using the moments of the millimeter-wavelength Doppler spectrum, *J. Geophys. Res.*, *107*(D24), 4815, doi:10.1029/2001JD001308.

Mace, G. G., Y. Zhang, S. Platnick, M. D. King, P. Minnis, and P. Yang (2005), Evaluation of cirrus cloud properties derived from MODIS data using cloud properties derived from ground-based observations collected at the ARM SGP site, *J. Appl. Meteorol.*, *44*, 221–240.

Matthews, G., K. Priestley, P. Spence, D. Cooper, and D. Walikainen (2005), Compensation for spectral darkening of short wave optics occurring on the Cloud's and the Earth's Radiant Energy System, Earth Observing Systems X, *Proc. SPIE*, 588212.

Minnis, P., W. L. Smith Jr., D. P. Garber, J. K. Ayers, and D. R. Doelling (1995a), Cloud properties derived from GOES-7 for the spring 1994 ARM Intensive Observing Period using version 1.0 of the ARM satellite data analysis program, *NASA RP 1366*, 59 pp.

Minnis, P., et al. (1995b), Cloud Optical Property Retrieval (Subsystem 4.3), in *Clouds and the Earth's Radiant Energy System (CERES) Algorithm Theoretical Basis Document*, vol. III, *Cloud Analyses and Radiance Inversions (Subsystem 4)*, *NASA Tech. Rep. RP 1376*, pp. 135–176.

Minnis, P., D. P. Garber, D. F. Young, R. F. Arduini, and Y. Takano (1998), Parameterization of reflectance and effective emittance for satellite remote sensing of cloud properties, *J. Atmos. Sci.*, *55*, 3313–3339.

Minnis, P., et al. (2004), Diurnal, seasonal, and interannual variations of cloud properties derived for CERES from imager data, in *Proc. 13th AMS Conf. Satellite Oceanogr. and Meteorol.* [CD-ROM], Norfolk, VA, 20–24 Sept., P6.10.

Minnis, P., D. R. Doelling, L. Nguyen, W. F. Miller, and V. Chakrapani (2008), Assessment of the visible channel calibrations of the TRMM VIRS and MODIS on *Aqua* and *Terra*, *J. Atmos. Oceanic Technol.*, in press.

Mishchenko, M. I., W. B. Rossow, A. Macke, and A. A. Lacis (1996), Sensitivity of cirrus cloud albedo, bidirectional reflectance and optical thickness retrieval accuracy to ice particle shape, *J. Geophys. Res.*, *101*(D12), 16,973–16,985.

Moran, K. P., B. E. Martner, M. J. Post, R. A. Kropfli, D. C. Welsh, and K. B. Widener (1998), An unattended cloud-profiling radar for use in climate research, *Bull. Am. Meteorol. Soc.*, *79*, 443–455.

Nasiri, S. L., B. A. Baum, A. J. Heymsfield, P. Yang, M. R. Poellot, D. P. Kratz, and Y. Hu (2002), The development of Midlatitude Cirrus Models for MODIS using FIRE-I, FIRE-II, and ARM in situ data, *J. Appl. Meteorol.*, *41*, 197–217.

Pilewskie, P., and F. P. J. Valero (1995), Direct observations of excess solar absorption by clouds, *Science*, *267*, 1626–1629.

Priestley, K. J., B. A. Wielicki, R. N. Green, M. P. A. Haeffelin, R. B. Lee, and N. G. Loeb (2002), Early radiometric validation results of the CERES Flight Model 1 and 2 instruments onboard NASA'S Terra Spacecraft, *Earth Atmos. Ocean Surf. Stud.*, *30*(11), 2371–2376, book series title: Advances In Space Research.

Ramanathan, V., B. Subasilar, G. J. Zhang, W. Conant, R. D. Cess, J. T. Kiehl, H. Grassl, and L. Shi (1995), Warm pool heat budget and shortwave cloud forcing: A missing physics?, *Science*, *267*, 499–503.

Rose, F., T. Charlock, Q. Fu, S. Kato, D. Rutan, and Z. Jin (2006), CERES proto-edition 3 radiative transfer: Tests and radiative closure over surface validation sites, peper presented at 12th Conference on Atmospheric Radiation (AMS), 10–14 July 2006, Madison, Wis.

Sherwood, S. C., J.-H. Chae, P. Minnis, and M. McGill (2004), Underestimation of deep convective cloud tops by thermal imagery, *Geophys. Res. Lett.*, *31*, L11102, doi:10.1029/2004GL019699.

Shi, Y., and C. N. Long (2002), Best estimate radiation flux value-added procedure: Algorithm operational details and explanations, *DOE ARM technical report TR-08*, (available online at http://www.arm.gov/publications/tech_reports/arm-tr-008.pdf)

Stamnes, K., S.-C. Tsay, W. Wiscombe, and K. Jayaweera (1988), Numerically stable algorithm for discrete-ordinate-method radiative transfer in multiple scattering and emitting layered media, *Appl. Opt.*, *27*, 2502–2509.

Stephens, G. L., and S. C. Tsay (1990), On the cloud absorption anomaly, *Q. J. R. Meteorol. Soc.*, *116*, 671–904.

Valero, F. P. J., R. D. Cess, M. Zhang, S. K. Pope, A. Bucholtz, B. Bush, and J. Vitko (1997), Absorption of solar radiation by clouds: Interpreta-

tion of collocated aircraft measurements, *J. Geophys. Res.*, *102*(D25), 29,917–29,927.

Valero, F. P. J., P. Minnis, S. K. Pope, A. Bucholtz, B. C. Bush, D. R. Doelling, W. L. Smith Jr., and X. Dong (2000), Absorption of solar radiation by the atmosphere as determined using satellite, aircraft, and surface data during the Atmospheric Radiation Measurement Enhanced Shortwave Experiment (ARESE), *J. Geophys. Res.*, *105*(D4), 4743–4758.

Wielicki, B. A., B. R. Barkstrom, E. F. Harrison, R. B. Lee III, G. L. Smith, and J. E. Cooper (1996), Clouds and the Earth's Radiant Energy System (CERES): An Earth observing system experiment, *Bull. Am. Meteorol. Soc.*, *77*, 853–868.

Wielicki, B. A., et al. (1998), Clouds and the Earth's Radiant Energy System (CERES): Algorithm overview, *IEEE Trans. Geosci. Remote Sens.*, *36*, 1127–1141.

Xiong, X., V. V. Salomonson, J. Kuyper, L. Tan, K. Chiang, J. Sun, and W. L. Barnes (2005), Status of the MODIS level 1B algorithms and calibration tables, *IEEE Int. Geosci. Remote Sens. Symp.*, *3*, 2231–2234.

Zender, C. S., B. Bush, S. K. Pope, A. Bucholtz, W. D. Collins, J. T. Kiehl, F. P. J. Valero, and J. Vitko Jr. (1997), Atmospheric absorption during the Atmospheric Radiation Measurement (ARM) Enhanced Shortwave Experiment (ARESE), *J. Geophys. Res.*, *102*(D25), 29,901–29,916.

S. Benson and G. G. Mace, Department of Meteorology, University of Utah, 135 S 1460 E, Rm 819, Salt Lake City, UT 84112-0110, USA.

T. Charlock, Y. Hu, S. Kato, P. Minnis, and B. A. Wielicki, MS 420, NASA Langley Research Center, Hampton, VA 23681-0001, USA.

X. Dong and B. Xi, Department of Atmospheric Sciences, University of North Dakota, 4149 University Dr. Stop 9006, Grand Forks, ND 58202-9006, USA. (dong@aero.und.edu)

F. Rose, Science Systems and Applications Incorporated (SSAI), Hampton, VA 23666, USA.